Equations and Electrochemical Methods for Measuring the Interfacial Charge-Transfer Kinetics of Li-ion Battery Active Materials at High Current Densities

Kevin Scanlan and Arumugam Manthiram*

Materials Science and Engineering Program & Walker Department of Mechanical Engineering

The University of Texas at Austin, Austin, TX 78712, USA

*Corresponding Author E-mail Address: rmanth@austin.utexas.edu

Keywords:

Lithium-ion batteries, electrochemical kinetics, impedance spectroscopy, charge-transfer resistance, transfer coefficient

Abstract

Experimental measurements and quantitative models of the interfacial charge-transfer kinetics of Li-ion battery (LIB) active materials (AM) are essential for accurate predictions of LIB rate performance, safety, and lifetime. The Butler-Volmer (BV) equation is commonly used to describe interfacial kinetics in LIBs as a function of the transfer coefficient (α) and exchange current (I_0). It is tacitly assumed that $\alpha \approx 0.5$, so experimental measurements of α for LIB AMs have rarely been attempted. In this work, mathematical models are derived to fit the apparent α and I_0 values from the electrochemical data at high current densities by reformulating the BV equation to describe the current dependence of charge-transfer resistance (R_{ct}) and differential charge-transfer resistance (R'_{ct}). Pseudo-steady-state extrapolation chronopotentiometry (S3E-CP), large-amplitude galvano EIS (LA-GEIS), and operando galvano EIS (O-GEIS) techniques are developed, and each is shown to be capable of accurately and precisely measuring the values of α and I_0 while maintaining the conditions of stability, stationarity, and linearity. Symmetric coin cells are demonstrated as a simple and widely accessible tool for achieving the most accurate kinetic measurements, and preliminary results are reported for $LiCoO_2$ symmetric cells at 50% state-of-charge. S3E-CP and LA-GEIS measurements yield apparent α values of, respectively, 0.420 and 0.431, while O-GEIS measurements show that these data are consistent with a two-step reaction with $\alpha_1 = 0.5$ and $\alpha_2 = 3$. The equations and electrochemical methods developed herein are broadly applicable for empirically measuring and modeling the interfacial charge-transfer kinetics in rechargeable batteries.

1. Introduction

Electrochemical kinetic measurements are a powerful tool for the development of Li-ion batteries (LIB) to meet the increasing performance requirements of demanding applications, such as electrified transportation. Accurate mathematical models of the electrochemical kinetics of LIB active materials (AM) and experimental methods for their parameterization are crucial for optimizing the pulse power, charging rate, wide-temperature operability, and safety of LIBs [1,2]. In particular, multi-scale electrochemical-thermal models which integrate a porous-electrode model (*i.e.*, P2D) at the stack level with thermal modeling at the cell and pack levels allows for the "virtual design" of LIBs, which can greatly reduce the experimental work required for battery development [3,4]. The measurement of electrochemical kinetics is also important for understanding and predicting the performance degradation of LIBs during cycling and calendar aging. For example, parasitic reactions between the electrolyte and AMs can cause severe interfacial impedance growth, especially at high temperatures, which poses a significant challenge for commercially relevant LIB AMs like layered oxide cathodes and silicon anodes [5,6].

The electrochemical kinetics of LIB AMs can generally be separated into bulk (*i.e.*, diffusion) kinetics and interfacial (*i.e.*, charge-transfer) kinetics, although in many cases these are highly interdependent. In the literature, the interfacial charge-transfer kinetics of LIB AMs are generally assumed to follow the Butler-Volmer equation (BV), which describes the relationship between current (I) and overpotential (η) based on two kinetic parameters, the exchange current (I_0) and the transfer coefficient (α). Based on the tacit assumptions that $\alpha \approx 0.5$ and $\alpha_a + a_c = 1$, the BV Equation is often formulated as [7,8]:

$$(1) \quad I = I_0 \left(\exp\left(\frac{\alpha F}{RT}\eta\right) - \exp\left(-\frac{(1-\alpha)F}{RT}\eta\right) \right)$$

https://doi.org/10.26434/chemrxiv-2024-hndjp ORCID: https://orcid.org/0000-0002-0257-3086 Content not peer-reviewed by ChemRxiv. License: CC BY 4.0

Accordingly, I_0 is typically calculated from the charge-transfer resistance (R_{ct}) measured with electrochemical impedance spectroscopy (EIS) under linearized conditions as [7]:

$$(2)\ R_{ct} = \frac{RT}{FI_0}$$

The fundamental feature of BV kinetics is that the current versus overpotential relationship is linear at small overpotentials but becomes exponential at large overpotentials. EIS measurements are advantageous because they are quick, non-destructive, and can deconvolute R_{ct} from other sources of resistance in the cell [9–11]. However, when EIS measurements are conducted within the linear region of BV kinetics (*i.e.*, at low overpotentials), it is impossible to directly measure the value of α or I_0, because infinitely many combinations of α and I_0 can yield the same R_{ct} value. Therefore, to experimentally measure α and I_0, the electrochemical measurements must be conducted in the non-linear region of BV kinetics (*i.e.*, at high current densities).

Electrochemical measurements of the interfacial kinetics of LIB AMs at high current densities (*i.e.*, > 10 mA cm^{-2}) have only rarely been reported in the literature [12–20]. Several electrochemical techniques have been employed for such measurements, including chronopotentiometry, chronoamperometry, cyclic voltammetry, and EIS. Other mathematical models besides the BV equation have also been proposed to fit the experimental data from these measurements [13,14,20]. In the literature, there are many conflicting reports, and there is not a clear consensus on the validity of the various experimental methods and theoretical models employed. In our previous work, it was found that the accuracy of some of these measurements from the literature may be questionable due to experimental errors, including uncompensated ohmic resistance and/or counter electrode polarization, or impedance artifacts causes by the counter and/or reference electrode in 3-electrode cells [18]. We also developed a novel pseudo-steady-state extrapolation (S3E) approach for Tafel analysis, which enables direct measurement of

4

the apparent BV kinetic parameters at high current densities through simple chronopotentiometry experiments. Surprisingly, it was found that LiFePO$_4$ (LFP) electrodes obey the BV equation with an apparent α value of ~ 1.5 for both the anodic and cathodic reactions, but due to "double Tafel slope" behavior arising from a non-uniform current distribution, the true α value for the interfacial charge-transfer reaction of LFP was shown to be ~ 3 [18]. This result is fundamentally inconsistent with the nearly universal assumption of $\alpha \approx 0.5$ in the literature, and with the classical theories of electron-transfer reactions on which this assumption is based [7,21]. In the context of this finding, and the lack of consensus in the literature, we believe it is necessary to critically re-examine the quantitative models and experimental methods which are used to measure the interfacial charge-transfer kinetics in LIBs.

Herein, mathematical models and electrochemical techniques are developed to measure the interfacial charge-transfer kinetics of LIB AMs at high current densities. First, a comprehensive treatment of Butler-Volmer kinetics is provided: starting with a generalized formulation of the BV equation, which assumes symmetry, but is agnostic to the specific reaction mechanism(s), a series of equations are derived which can be used to fit the apparent values of α and I$_0$ from the experimental electrochemical data. Specifically, equations are developed to describe the dependence of charge-transfer resistance and differential charge-transfer resistance on current density. We develop three electrochemical techniques for interfacial kinetic measurements at high current density: pseudo-steady-state extrapolation chronopotentiometry (S3E-CP), large-amplitude galvano EIS (LA-GEIS), and operando galvano EIS (O-GEIS). We discuss in detail the practical considerations of conducting electrochemical kinetic measurements at high current densities, and quantitatively show that each technique is capable of accurately and precisely measuring the values of α and I$_0$ while satisfying the necessary conditions of stability, stationarity,

5

and linearity. Lithium cobalt oxide ($LiCoO_2$) symmetric cells are used as an exemplary model system to demonstrate the theory and methods developed in this work, and preliminary measurement results are reported and discussed.

2. Experimental Procedures

2.1. Active Materials Synthesis, Electrode Fabrication, and Cell Assembly

The complete experimental details on active material synthesis, electrode coating, and cell materials and assembly are provided in the supplemental information. Briefly, lithium cobalt oxide (LCO) was synthesized with a nominal composition of $LiCo_{0.97}Al_{0.02}Ti_{0.005}Mg_{0.005}O_2$ through a molten salt reaction with a sodium sulfate flux, yielding single-crystal particles with an average size of ~ 3 μm. LCO electrodes were prepared by slurry coating onto carbon-coated Al foil. The coatings had a composition of 97.5 wt% AM, 1.0 wt% poly(vinylidene difluoride), 1.0 wt% carbon black, and 0.5 wt% vapor-grown carbon nanofibers. The electrode coatings had mass loadings of $1.2 - 1.4$ mg cm^{-2} and were calendared to a density of $3.9 - 4.1$ g cm^{-3} to achieve a coating thickness of ~ 3 μm. The electrolyte used for all experiments was 1.2 M $LiPF_6$ + 0.1M $LiPO_2F_2$ + 0.1M lithium 4,5-dicyano-2-trifluoromethylimidazole (LiTDI) in a 25 : 75 w/w mixture of fluoroethylene carbonate (FEC) : dimethyl carbonate (DMC).

Coin cells were built with CR2032 cases and contained a wave spring, a top (1 mm thick) and bottom (0.6 mm thick) Al spacer (both 16.2 mm diameter), one ¾" diameter ceramic-coated polyolefin separator (Celgard, H1409, 14 μm), 40 μL of electrolyte, and two 16 mm diameter LCO electrodes. For each symmetric cell, the two electrodes were paired to ensure they had a nearly identical mass (< 2% difference). Symmetric cells with pristine LCO electrodes were assembled to measure the pore resistance of the electrodes under blocking conditions. LCO symmetric cells

6

with electrochemically delithiated LCO electrodes were prepared by pre-cycling the LCO electrodes versus Li-metal counter electrodes in Swagelok cells. The LCO was charged at a ~ 2C rate to 4.15 V vs. Li/Li$^+$, then held at 4.15 V until a C/50 current cutoff. After extracting the electrodes from Swagelok cells, they were rinsed thoroughly with DMC and dried under vacuum to remove the residual solvent, then two delithiated LCO electrodes were used to build a symmetric coin cell with fresh electrolyte.

2.2. Electrochemical Techniques

All electrochemical measurements were conducted on LCO symmetric cells, which contained electrodes with a mass loading of ~ 1.3 mg cm^{-2}. The electrodes were either pristine (blocking condition) or charged to 4.15 V vs. Li/Li$^+$ (intercalating condition), corresponding to ~ 50% state-of-charge (SOC). The cells were housed in a temperature chamber with 0.1 °C precision (Espec), and unless otherwise stated, measurements were taken at 25.0 °C. A Biologic VMP-300 potentiostat was used for all measurements. The EIS Quality Indicators option in EC-LAB software was enabled, which calculates the total harmonic distortion (THD) and non-stationary distortion (NSD) for every EIS measurement. Potential-controlled EIS (PEIS) was conducted with a 10 mV excitation amplitude about a constant cell voltage of 0 V. Pore resistance (R_p) of the electrodes was measured with the PEIS of symmetric cells under blocking conditions in the frequency range of 500 kHz – 10 Hz. Linearized charge-transfer resistance (R_{ct}^0) was measured with PEIS of symmetric cells under intercalating conditions in the frequency range of 500 kHz – 1 Hz. The values of R_p and R_{ct}^0 were fitted from the Nyquist data with Morasch's method [22]. Specifically, for both blocking and intercalating conditions, the solution resistance (R_s) was calculated by a linear interpolation of the high-frequency (HF) intercepts of the Nyquist plots. R_p was quantified under blocking conditions by a linear extrapolation of the Nyquist data at 250 –

7

2500 Hz to calculate the low-frequency (LF) intercept; the difference between the HF and LF intercepts is equal to $R_p/3$. The value of R_p measured under blocking conditions was used to calculate the ohmic resistance (R_Ω) used for IR compensation of the kinetic measurements. For impedance measurements, $R_\Omega = R_s + R_p/3$, while for direct-current measurement, $R_\Omega = R_s + R_p$. For PEIS and LA-GEIS measurements, R_{ct} was quantified by subtracting R_Ω from the real impedance at the LF touchdown point of the semicircle. The touchdown point was interpolated from the Nyquist data by calculating dZ_{Im}/dZ_{re} for each point, then applying quadratic interpolation of the 7 points centered around the minimum value of dZ_{Im}/dZ_{re}. For PEIS and O-GEIS measurements, R_{ct} was also quantified by fitting the Nyquist data to an equivalent-circuit model with Biologic EC-Lab software.

Pseudo-steady-state extrapolation chronopotentiometry (S3E-CP) was conducted by applying a series of short galvanostatic pulses with current density ranging from 5 to 100 mA cm^{-2} with 10 points per decade in logarithmic spacing. Each pulse was terminated at a capacity limit of 15 µAh cm^{-2} (~ 10% SOC) and voltage data were recorded every 0.05 µAh cm^{-2}. Immediately after each pulse, the cell was held at an applied voltage of 0 V to reset the open circuit voltage (OCV) and allow the cell to cool between measurements. The rest time varied with current density, ranging from 3 min at 5 mA cm^{-2} to 30 min at 100 mA cm^{-2}. PEIS data were taken after each rest step to ensure stability of the measurements. For each pulse, a linear fit was applied between a capacity range of 6 and 13.5 uAh cm^{-2} to calculate the intercept at zero capacity, which gives the extrapolated pseudo-steady state voltage for each current density. The IR drop was subtracted from the voltage versus current data based on the value of R_Ω measured with PEIS, and the residual was divided by two to give the overpotential of a single electrode. The overpotential versus current

8

data were fitted to both a BV model (Eq. 9-13) and a Tafel model (Eq. 14). Excel Solver was used to fit the apparent values of α and I_0 with least-squares error minimization.

LA-GEIS measurements were collected with a single impedance scan for each spectrum, with 9 – 11 points per scan (4 – 6 s scan time). The excitation current amplitude ranged from 1 to 100 mA cm^{-2} with 10 points per decade in logarithmic spacing. The frequency range was varied with current density from 1 – 10 Hz at 1 mA cm^{-2}, to 3 – 15 Hz at 100 mA cm^{-2}. The data for each scan were collected from low to high frequency with no averaging and with a 0.1 period wait time between each frequency. The rest time between scans varied from 1 min at 1 mA cm^{-2} to 10 min at 100 mA cm^{-2}. The value of R_{ct} was calculated by quadratic interpolation of the semicircle touchdown point. The root-mean-square (RMS) current during LA-GEIS is equal to $1/\sqrt{2}$ times the current excitation amplitude. The R_{ct} versus RMS current data were fitted to Eq. 13 with least-squares error minimization (Excel Solver) to fit the value of I_0, and the value of α was calculated from Eq. 7. To ensure the condition of the linearity, LA-GEIS data were fitted only within the current range where the THD was < 2%. Preliminary LA-GEIS measurements, which were not used for quantitative analysis, were also conducted. The preliminary data were collected with a single point per scan (~ 0.5 s scan), a 5 min rest between each scan, a frequency range of 1 Hz – 100 kHz, and current excitation amplitudes ranging from 1 – 250 mA cm^{-2}.

O-GEIS measurements were conducted with a single impedance point per scan without averaging between a frequency range of 100 – 794 Hz. The applied current density ranged between 5 – 25 mA cm^{-2} with 10 points per decade in logarithmic spacing, and the current excitation amplitude was 10% of the applied current density, ranging from 0.5 – 2.5 mA cm^{-2}. The drift correction option in the EC-Lab software was enabled to compensate for changes in the cell voltage during measurements. Between each scan, the cell was held at 0 V to reset the OCV and allow for

cooling. The rest time ranged from 2 min at 5 mA cm^{-2} to 5 min at 25 mA cm^{-2}. The differential charge-transfer resistance (R'_{ct}) at each current density was calculated by an equivalent-circuit-model fit of the impedance data between a frequency of 100 and 794 Hz to an equivalent circuit of $Z = R_\Omega + R_{ct}/Q$, with the value of R_Ω determined from PEIS under blocking conditions. The R'_{ct} versus current data were fitted to a one-step BV model (Eqs. 39-40) by least-squares error minimization (Excel Solver) to fit the value of I_0, and the value of α was calculated from Eq. 7. The data were also fitted to a two-step BV model (Eqs. 23 and 39), assuming $\alpha_1 = 0.5$ and $\alpha_2 = 3$, to calculate the values of $I_{0,1}$ and $I_{0,2}$ by least-squares error minimization.

To measure the direct-current voltage response of the cell during LA-GEIS and O-GEIS measurements, two potentiostat channels were connected in parallel; one channel ran the EIS measurement and the other channel measured the OCV every 0.2 ms. The magnitudes of the voltage harmonics were calculated from the discrete Fourier transform of the voltage versus time data with EC-Lab software. Large amplitude sinusoidal voltammetry (LASV) was conducted at a frequency of 10 Hz between a voltage of -1 V to 1 V, and the data are shown for the 2nd -10th cycle.

3. Theory and Calculation

3.1. Introduction to the Butler-Volmer Equation

The BV equation can be written in many different notations, depending on the underlying assumptions made. For example, the form of the BV equation given by Bard and Faulkner (Eq. 1) assumes the interfacial reaction to be an elementary one-step, single-electron reaction with electron-transfer as the rate-determining step, so the transfer coefficient is assumed to be $\alpha_a + \alpha_c = 1$ [7]. However, in real electrochemical systems, complex multi-step interfacial reactions can occur, where the apparent (*i.e.*, experimentally measured) value of α can differ from the intrinsic

α value(s) for the individual reaction step(s) [23,24]. The measured α value can also be strongly influenced by porous electrode phenomena [1,18,25]. As strictly defined by IUPAC, the transfer coefficient is a directly determined experimental quantity, the value of which can only be obtained by measuring the relationship between current and overpotential at high overpotentials (*i.e.*, from the Tafel slope), according to [24]:

$$(3)\ \alpha \equiv \left(\frac{RT}{F}\right)\left(\frac{d\ln I}{d\eta}\right)$$

It must be clearly emphasized that all the equations and methods developed in this work relate purely to the experimental measurement of the apparent α value as defined by Eq. 3; as such, they are valid for any positive values of α and I_0 and are entirely agnostic to the specific reaction mechanism(s). Accordingly, we begin with a generalized form of the BV equation, which accounts for asymmetry of both the exchange current (I_0) and transfer coefficient (α) between the anodic (a) and cathodic (c) directions [8]:

$$(4)\ I = I_{0,a}\exp\left(\frac{\alpha_a F}{RT}\eta\right) - I_{0,c}\exp\left(\frac{\alpha_c F}{RT}\eta\right)$$

where I is the current and η is the overpotential. The values of α and I_0 in Eq. 4, and all equations derived from it, are treated purely as unknown empirical parameters, which must be fitted from the experimental electrochemical data. In this notation, both the temperature and concentration dependence of the interfacial kinetics are included in the terms for the exchange current.

The mathematics of the BV equation can be greatly simplified if the kinetics are assumed to be symmetric between the anodic and cathodic directions [7]. As will be discussed in detail later (Section 4.2), the experimental methods can also be simplified, and the accuracy of the experimental data can be ensured, by conducting electrochemical kinetic measurements in symmetric cells. In this case, even if the interfacial kinetics of the AM are asymmetric (*e.g.*, $\alpha_a \neq \alpha_c$), the measured voltage versus current data of the symmetric cell are necessarily symmetric:

11

because the two electrodes are in series, as one electrode undergoes the anodic reaction at a certain current density, the other electrode simultaneously undergoes the cathodic reaction at the same current density. The apparent transfer coefficient measured in a symmetric cell is approximately the average value between the anodic and cathodic directions:

$$(5) \ \alpha \approx (\alpha_a + \alpha_c)/2$$

If the measured interfacial kinetics are assumed to be symmetric between the anodic and cathodic directions (*i.e.*, $I_0 = I_{0,a} = I_{0,c}$ and $\alpha = \alpha_a = \alpha_c$), then Eq. 4 can be simplified to [7,16,20]:

$$(6) \ I = 2I_0 \sinh\left(\frac{\alpha f}{RT}\eta\right)$$

3.2. Resistance vs. Current Notation of the Butler-Volmer Equation

The interfacial-charge transfer kinetics in LIB AMs ultimately manifest as, and can only be measured by, the electrical resistance within the battery cell. As such, it is convenient to characterize the interfacial kinetics in units of resistance (*i.e.*, Ω cm^2). In the literature, the interfacial charge-transfer resistance (R_{ct}) is typically measured with electrochemical impedance spectroscopy (EIS) by applying a sufficiently small voltage excitation (*e.g.*, < 10 mV) to ensure that the kinetics remain in the linear region [11,26,27]. For clarity, we refer to the value of R_{ct} measured within the linear region of the kinetics as the linearized charge-transfer resistance (R_{ct}^0), which for a one-step reaction can be calculated from α and I_0 according to [7,8]:

$$(7) \ R_{ct}^0 = \frac{RT}{2\alpha F I_0}$$

However, it must be emphasized that since there are infinitely many combinations of α and I_0 which yield the same value of R_{ct}^0, it is fundamentally impossible to directly measure α or I_0 within the linear region of the kinetics. Measurements of α and I_0 must, therefore, be conducted within the non-linear region of the kinetics (*i.e.*, at high current densities).

According to Ohm's law, R_{ct} can be defined for any non-zero value of current as the ratio between overpotential and current:

(8) $R_{ct} \equiv \eta/I$

Eq. 6 can be analytically solved for the overpotential, giving:

(9) $\eta = \left(\frac{RT}{\alpha F}\right) \sinh^{-1}\left(\frac{I}{2I_0}\right)$

For one-step symmetric kinetics, the BV equation can be reformulated to describe the current dependence of the charge-transfer resistance [16,20]:

(10) $R_{ct} = \left(\frac{RT}{\alpha F}\right)\left(\frac{1}{I}\right) \sinh^{-1}\left(\frac{I}{2I_0}\right)$

A dimensionless resistance (r) and a dimensionless current (i) can also be defined as:

(11) $r \equiv R_{ct}/R_{ct}^0$

(12) $i \equiv I/2I_0$

Upon inserting Eq. 7 and substituting the dimensionless variables, Eq. 10 can be rewritten in a simplified dimensionless notation:

(13) $r = i^{-1} \sinh^{-1}(i)$

Importantly, Eq. 13 reveals that regardless of the specific values of α and I_0, there is a universal dimensionless relation between charge-transfer resistance and current density for one-step symmetric BV kinetics.

As an example, Fig. 1A-B shows the calculated overpotential versus current behavior (*i.e.*, Tafel plots) for one-step symmetric BV kinetics with different values of *α* or *I₀*; Fig. 1C-H shows the same data in the resistance notation given by Eq. 10. From the Tafel plots, we observe the familiar behavior of BV kinetics: *I₀* essentially describes the current above which the kinetics enter the non-linear region, while *α* describes the rate at which overpotential scales with current (*i.e.*,

13

the Tafel slope) within the non-linear region. The Tafel slope (b), in volts per decade, is related to α according to [7]:

(14) $\quad b = \dfrac{RT \ln 10}{\alpha F}$

The resistance versus current plots reveal that R_{ct} is constant and equal to R_{ct}^0 within the linear region (*i.e.*, $I < I_0$). However, R_{ct} begins to decrease once the current approaches I_0, and R_{ct} decays logarithmically with current within the non-linear region (*i.e.*, $I > I_0$). It is evident that I_0 greatly affects both the magnitude of R_{ct}^0 and the current dependence of R_{ct}, while α affects only the magnitude of R_{ct} (Fig. 1 C-D). The current dependence of R_{ct} can be better understood by plotting the normalized charge-transfer resistance (r) versus either current or overpotential (Fig. 1E-H). Regardless of the value of I_0, the kinetics begin to enter the non-linear region at a fixed overpotential, which can be referred to as the exchange voltage (V_0):

(15) $\quad V_0 = I_0 R_{ct}^0 = \dfrac{RT}{2\alpha F}$

In other words, because R_{ct}^0 is inversely proportional to I_0, a higher linearized resistance causes the exchange voltage to be reached at a proportionally lower exchange current. From these observations, it can be understood that the non-linearity of BV kinetics manifests as a decrease in charge-transfer resistance with increasing current above $I > I_0$, and that the overpotential is the true driving force of this non-linearity. Additionally, for any values of α and I_0, it can be proven that R_{ct} approaches zero at extremely high current density, according to:

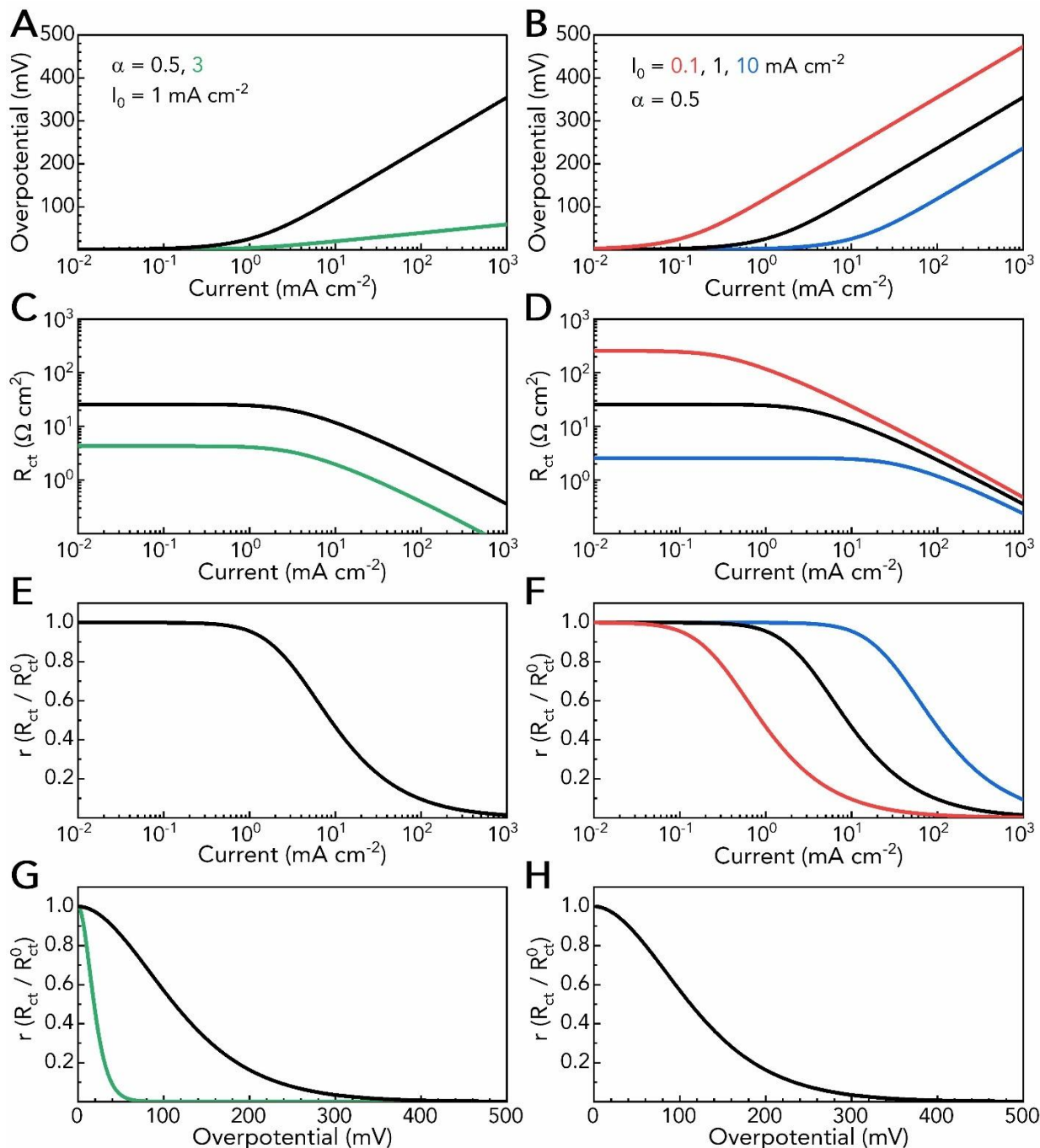(16) $\quad \lim\limits_{i \to \infty} (i)^{-1} \sinh^{-1}(i) = 0$

Figure 1. Current dependence of charge-transfer resistance for symmetric BV kinetics.
Mathematical models of symmetric Butler-Volmer kinetics showing **(A-B)** overpotential (η) versus current (*I*), **(C-D)** charge-transfer resistance (R_{ct}) versus current, **(E-F)** normalized charge-transfer resistance ($r = R_{ct} / R^0_{ct}$) versus current, and **(G-H)** normalized charge-transfer resistance versus overpotential. Calculations are performed **(A, C, E, G)** for an exchange current of 1 mA cm^{-2} and a transfer coefficient of 0.5 or 3, and **(B, D, F, H)** for a transfer coefficient of 0.5 and an exchange current of 0.1, 1, or 10 mA cm^{-2}.

3.3. Differential and Linearized Charge-Transfer Resistance

In the same way that BV kinetics can be linearized at small overpotentials (*i.e.*, about a current of zero), the kinetics can also be linearized about any value of applied current, even within the non-linear region of the kinetics. The slope of the overpotential versus current curve has units of resistance ($R = V/I$). The charge-transfer resistance (R$_{ct}$) can be visualized as the average slope of the overpotential versus current curve between the origin and the applied current (Fig. 2A). By extension, the differential charge-transfer resistance can be visualized as the local slope (dV/dI) of the overpotential versus current curve at any point (I, η) on the curve. Similarly, the linearized charge-transfer resistance (R_{ct}^0) can be visualized as the local slope of the overpotential versus current curve at a current of zero. The differential charge-transfer resistance (R_{ct}') can be formally defined as the rate of change of overpotential with respect to current:

(17) $\ R'_{ct} \equiv d\eta/dI$

Exact expressions for R_{ct}' can be obtained by differentiation of the steady-state overpotential versus current relationship with respect to current, which for one-step symmetric BV kinetics (Eq. 9) yields:

(18) $\ R'_{ct} = \left(\frac{RT}{2\alpha F I_0}\right)\left(1 + \left(\frac{I}{2I_0}\right)^2\right)^{-\frac{1}{2}}$

Since R_{ct} is undefined at a current of zero from Eq. 8, the linearized charge-transfer resistance (R_{ct}^0) must be defined as the limit of the differential charge-transfer resistance as the current approaches zero:

(19) $\ R_{ct}^0 \equiv \lim_{I \to 0} R'_{ct}$

Evaluating this limit for Eq. 18 yields the same expression for R_{ct}^0 as given by Eq. 7. The current dependence of R_{ct}' can also be expressed in a simplified dimensionless notation as:

16

(20) $\; r' = R'_{ct}/R^0_{ct}$

(21) $\; r' = (1 + i^2)^{-\frac{1}{2}}$

Notably, the charge-transfer resistance (Eq. 10) and differential charge-transfer resistance (Eq. 21) follow a different current dependence, with R'_{ct} decreasing much more sharply with increasing current than R_{ct} (Fig. 2B).

The above equations reveal that R_{ct}, R'_{ct}, and R^0_{ct} represent three distinct types of charge-transfer resistances, and each of these is a real physical quantity, which can be experimentally measured with the appropriate electrochemical techniques. As an example, Fig. 2C-D shows the calculated current and voltage versus time data for: PEIS with a 10 mV excitation, LA-GEIS with a 100 mA cm^{-2} excitation, S3E-CP with a 100 mA cm^{-2} applied current, and O-GEIS with a 100 mA cm^{-2} applied current and a 10% (10 mA cm^{-2}) excitation. The calculations assume symmetric BV kinetics with $\alpha = 0.5$ and $I_0 = 1$ mA cm^{-2}. Direct-current techniques like S3E-CP can be used to measure the value of R$_{ct}$ as a function of applied current. R$_{ct}$ can also be measured by LA-GEIS, but due to the periodic nature of impedance measurements, LA-GEIS technically measures the root-mean-square (RMS) value of the charge-transfer resistance during the sinusoidal excitation [28]. R^0_{ct} can be measured with EIS using a sufficiently low amplitude excitation (of either voltage or current) applied about the equilibrium voltage of the cell. R'_{ct} can be measured with O-GEIS by calculating the impedance response to a small-amplitude sinusoidal excitation, which is superimposed on a large applied direct current bias.
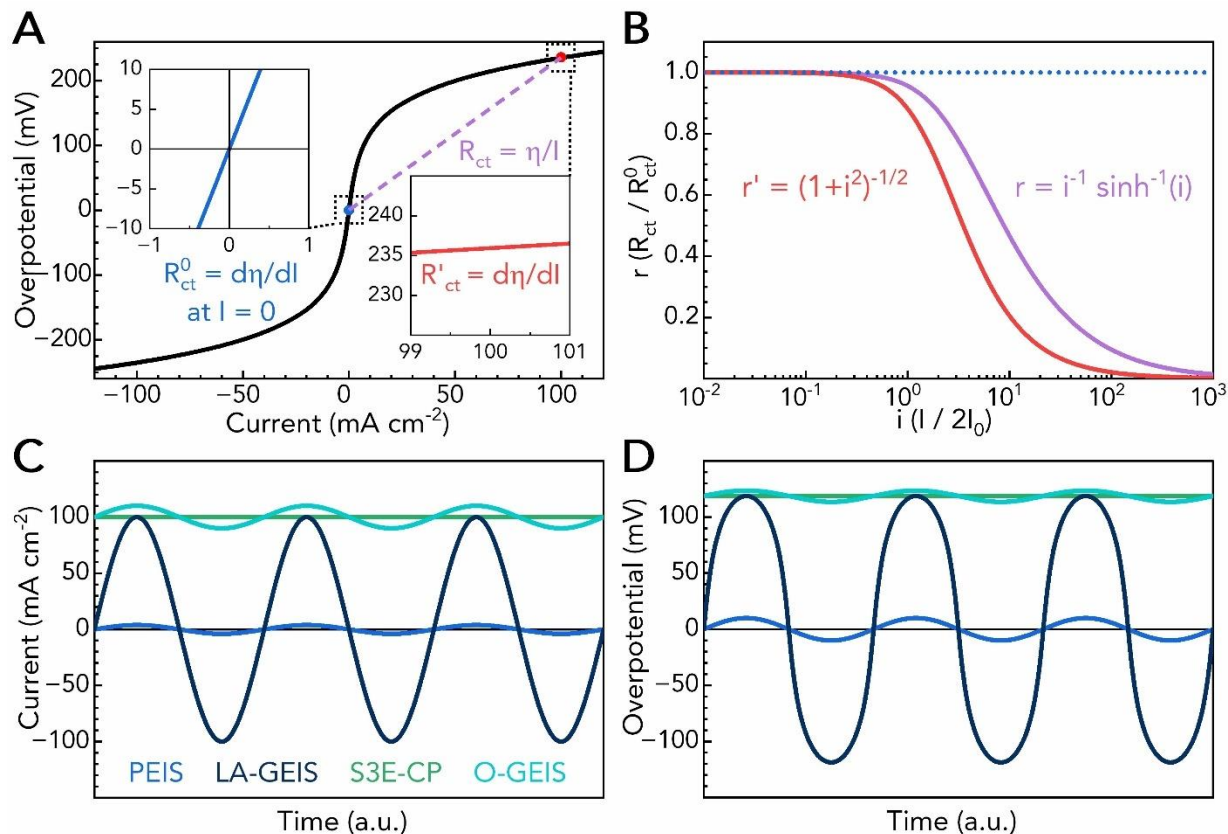
17

Figure 2. Electrochemical methods for measuring R$_{ct}$ and R'$_{ct}$ at high current densities.
(A) Calculated overpotential versus current data for symmetric BV kinetics ($\alpha = 0.5$, $I_0 = 1$ mA cm^{-2}), showing how charge-transfer resistance (R_{ct}), differential charge-transfer resistance (R'_{ct}), and linearized charge transfer resistance (R^0_{ct}) are measured from the slope of the overpotential versus current curve. R^0_{ct} is the local slope at $I = 0$, R'_{ct} is the local slope at the applied current, and R_{ct} is the average slope between $I = 0$ and the applied current. **(B)** Dimensionless plots of normalized resistance ($r = R_{ct} / R^0_{ct}$) versus normalized current ($i = I / 2I_0$), showing the universal relationships of R_{ct} and R'_{ct} with current. **(C-D)** Calculated current and overpotential versus time data for PEIS with a 10 mV excitation, LA-GEIS with a 100 mA cm^{-2} excitation, S3E-CP with a 100 mA cm^{-2} applied current, and O-GEIS with a 100 mA cm^{-2} applied current and a 10 mA cm^{-2} excitation.

18

3.4. Multi-Step Reactions

Interfacial charge-transfer reactions in electrochemical systems often involve multiple reaction steps [7]. For multi-step reactions, the experimentally measured (*i.e.*, apparent) α value is understood to be a compound parameter, which can be different than the α values of each elementary reaction step [24]. The mechanisms of multi-step electron-transfer reactions can often be understood through analysis of the apparent α value, for example, by the quasi-equilibrium method [7,23]. However, it must be reiterated that the equations developed in this work are related purely to the experimental measurement of the apparent α value, and should not be construed to imply any mechanistic conclusions about the apparent α value. It must also be recognized that the empirical models derived so far, which assume one-step symmetric BV kinetics, may not provide a sufficiently accurate description of the interfacial kinetics for multi-step reactions. For the sake of mathematical simplicity, we assume that the interfacial kinetics can be fully described by the BV equation, but this assumption is understood not to be universally valid for real electrochemical systems. For example, there are many reported cases of elementary steps in multi-step reactions (*e.g.*, coupled chemical reactions) which do not follow the BV equation; this can, but does not necessarily, cause the measured interfacial kinetics to deviate from the BV equation [7,23]. If the measured kinetics of at least one reaction step is to deviate from the BV equation, this deviation would manifest as a quantitative disagreement between the experimental data and the mathematical models developed herein, in which case alternative models would be needed to fit the empirical data. However, no such disagreement is observed in the present work.

We, therefore, assume that the experimentally measured interfacial kinetics can be described by a series of n observed reaction steps, each of which obeys symmetric BV kinetics (Eq. 6) with arbitrary values of α_n and $I_{0,n}$, according to:

19

(22) $I_n = 2I_{0,n} \sinh\left(\frac{\alpha_n F}{RT}\eta\right)$

The quasi-equilibrium assumption is often used to describe the kinetics of multi-step reactions in terms of a single rate-determining step (RDS), but this assumption is only valid when the rate constant (*i.e.*, I_0) for the RDS is at least 100 times lower than that for all the preceding steps, a condition which cannot be generally assumed [23,24]. Alternatively, the steady-state assumption can be adopted: under constant current, it can be assumed that the effective concentrations of all intermediate species in the multi-step reaction approach steady-state values at sufficiently long timescales (*i.e.*, at low frequencies) [23,24]. Under this assumption, the current must be equal for each reaction step ($I = I_n$), so the total charge-transfer resistance for a multi-step reaction with n steps in series is equal to the sum of the resistances of each step:

(23) $R_{ct} = \sum_n R_{ct,n}$

From Ohm's law, the total overpotential is likewise the sum of the overpotentials of each step:

(24) $\eta = \sum_n \eta_n$

Assuming all reaction steps follow one-step symmetric BV kinetics, the expressions for the total overpotential, charge-transfer resistance, differential charge-transfer resistance, and linearized charge-transfer resistance for a multi-step reaction are given by the summations:

(25) $\eta = \left(\frac{RT}{F}\right) \sum_n \left\{ (\alpha_n)^{-1} \sinh^{-1}\left(I/2I_{0,n}\right) \right\}$

(26) $R_{ct} = \left(\frac{RT}{F}\right)\left(\frac{1}{I}\right) \sum_n \left\{ (\alpha_n)^{-1} \sinh^{-1}\left(I/2I_{0,n}\right) \right\}$

(27) $R'_{ct} = \left(\frac{RT}{2F}\right) \sum_n \left\{ (\alpha_n I_{0,n})^{-1} \left(1 + \left(I/2I_{0,n}\right)^2\right)^{-\frac{1}{2}} \right\}$

(28) $R^0_{ct} = \left(\frac{RT}{2F}\right) \sum_n \left\{ (\alpha_n I_{0,n})^{-1} \right\}$

where α_n and $I_{0,n}$ are, respectively, the transfer coefficient and exchange current for the nth reaction step.

At low current densities ($I \ll I_{0,n}$ for all n), all reaction steps will be in the linear region of BV kinetics. As in the case of a one-step reaction, there are infinitely many combinations of α_n and $I_{0,n}$ which give the same value of $R_{ct,n}^0$, so kinetic measurements within the linear region cannot discern the values of α or I_0, nor whether the reaction is one-step or multi-step. At high current densities ($I \gg I_{0,n}$ for all n), all the reaction steps will be in the Tafel region with an apparent Tafel slope of:

$$(29) \quad b = \frac{RT \ln 10}{F} \sum_n (\alpha_n)^{-1}$$

Therefore, the apparent values of α and I_0 measured for a multi-step reaction at sufficiently high current density are:

$$(30) \quad \alpha = \left(\sum_n (\alpha_n)^{-1} \right)^{-1}$$

$$(31) \quad I_0 = \left(\frac{RT}{2FR_{ct}^0} \right) \sum_n (\alpha_n)^{-1}$$

At either very low or very high current densities, a multi-step reaction is expected to behave analogously to a single-step reaction with these apparent values of α and I_0. Under such conditions, it is impossible to directly measure the α value for each reaction step, since the same apparent α value can be described by infinitely many combinations of α_n. Nonetheless, these equations can still be used to constrain the possible values of α_n for each reaction step, which are consistent with the apparent α value. For example, for a two-step reaction with $\alpha_1 = 0.5$ and $\alpha_2 = 3$, the apparent α value would be 3/7 (0.4285).

As an example, Fig. 3 shows modeling of the charge-transfer resistance (Fig. 3A,C,E) and differential charge-transfer resistance (Fig. 3B,D,E) for one-step and two-step reactions following symmetric BV kinetics. Data are shown for Step 1 having $\alpha_1 = 0.5$ and $I_{0,1} = 1$ mA cm^{-2}, and Step 2 having $\alpha_2 = 3$ and $I_{0,2}$ values ranging from 0.01 – 10 mA cm^{-2}. Fig. 3A-B shows $R_{ct,n}$ and $R'_{ct,n}$ for each individual reaction step, while Fig. 3C-D shows the total R_{ct} and R'_{ct} for the two-step

reactions (colored lines) compared to that of Step 1 only (black line). When $I_{0,2} \gg I_{0,1}$, the magnitude of $R_{ct,2}$ is negligible compared to $R_{ct,1}$, and $R_{ct,2}$ does not begin to decrease until a much higher current density. When $I_{0,2} = I_{0,1}$, the magnitude of $R_{ct,2}$ is proportionally smaller than $R_{ct,1}$ due to the larger α value, but both steps follow the same current dependence. When $I_{0,2} \ll I_{0,1}$, the magnitude of $R_{ct,2}^{0}$ is much greater than $R_{ct,1}^{0}$, but $R_{ct,2}$ begins to decrease at a much lower current density than $R_{ct,1}$. Consequently, even when $I_{0,2}$ is 100 times lower than $I_{0,1}$, the magnitude of $R_{ct,2}$ becomes lower than $R_{ct,1}$ at a relatively low current density of ~ 3 mA cm^{-2}.

Overall, depending on the relative magnitudes of $I_{0,n}$ for each step, several limiting cases can emerge with different implications to the measured α value. When $I_{0,2} \gg I_{0,1}$, $R_{ct,2}$ is much smaller than $R_{ct,1}$ across the entire current range, and the two-step reaction behaves like a one-step reaction with $\alpha = 0.5$. When $I_{0,2} = I_{0,1}$, the two-step reaction behaves as a one-step reaction with $\alpha = 0.4285$. When $I_{0,2} \ll I_{0,1}$, more complex behavior emerges at low current density, where $R_{ct,2}$ decreases significantly with current, while $R_{ct,1}$ remains essentially constant until $I > I_{0,1}$. When the difference between $I_{0,1}$ and $I_{0,2}$ is large, a "plateau" in the resistance versus current plots can emerge in the current range between $I_{0,1}$ and $I_{0,2}$. Because R_{ct}' decreases more quickly with current than R_{ct}, the differential charge-transfer resistance provides a more pronounced separation between the resistance versus current features for each reaction step. Comparing the normalized R_{ct} and R_{ct}' versus current curves for a two-step reaction with relatively small differences between $I_{0,1}$ and $I_{0,2}$, it is evident that differential resistance measurements can resolve much larger changes in the magnitude of resistance, and in the shape of the resistance versus current curve (Fig. 2E-F). In summary, at either very low or very high current densities, or when $I_{0,1} = I_{0,2}$, a two-step reaction will be indistinguishable from a one-step reaction, but the apparent α value can still indicate the possibility of a two-step reaction. Additionally, differential-charge transfer resistance

22

measurements at intermediate current densities appear to be a suitable tool for directly deconvoluting the resistance contributions of multiple reaction steps in series, even when the exchange currents are similar.
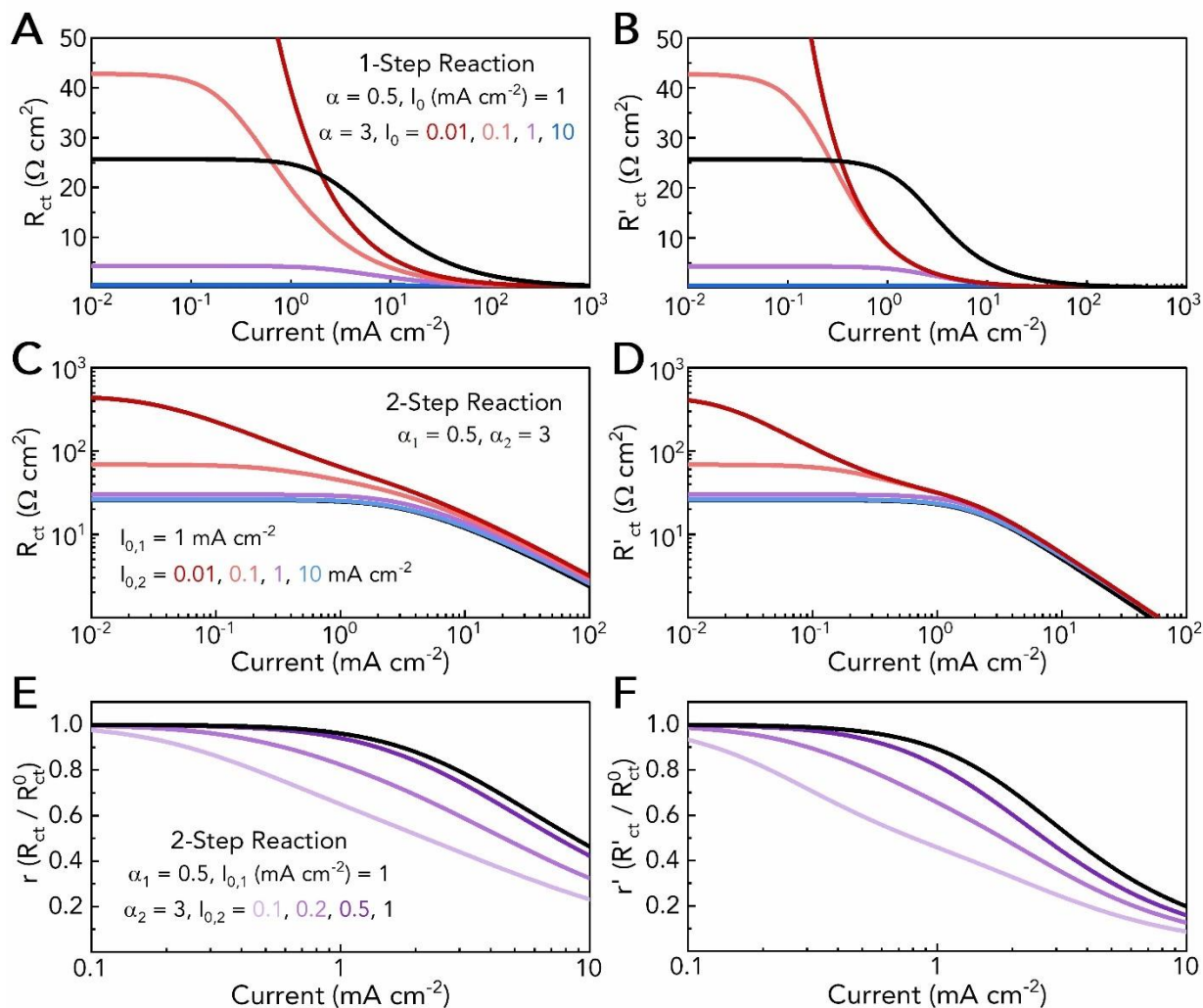

Figure 3. Current dependence of R$_{ct}$ and R'$_{ct}$ multi-step symmetric BV kinetics.
Mathematical models of symmetric Butler-Volmer kinetics, showing **(A,C,E)** charge-transfer resistance (R_{ct}) and **(B,D,F)** differential charge-transfer resistance (R'_{ct}) versus current for **(A-B)** one-step reactions and **(C-F)** two-step reactions with different values of α and I_0. The first step (black curve) is kept constant with $\alpha_1 = 0.5$ and $I_{0,1} = 1$ mA cm^{-2}. The second step has $\alpha_2 = 3$, and has $I_{0,2}$ values ranging from **(A-D)** 0.01 – 10 mA cm^{-2} or **(E-F)** 0.1 – 1 mA cm^{-2}.

3.5. Ohmic Resistance

The total measured resistance of the cell (R) is equal to the sum of the ohmic resistance (R_Ω) and the charge-transfer resistance (R_{ct}) [7]:

$$(32) \quad R = R_\Omega + R_{ct}$$

Since the ohmic resistance does not change with current, the measured differential resistance (R') of the cell can be expressed analogously:

$$(33) \quad R' = R_\Omega + R'_{ct}$$

The measured cell voltage under direct current conditions is given by:

$$(34) \quad V = IR_\Omega + \eta(I)$$

Fig. 4 shows, in various representations of the data, how the ohmic resistance of the cell affects the measured cell polarization and resistance. Even a small ohmic resistance of 1 Ω cm^2 can have a significant impact on the current versus voltage relation at high current densities, resulting in the appearance of "deformed Tafel plots", which have sometimes been observed in the literature (Fig. 4A-B) [13,14,20]. When $R_\Omega \gg R_{ct}^0$, the BV kinetics become completely obscured and the voltage versus current relation becomes essentially ohmic. At very high current densities, as the value of R_{ct} approaches zero, the cell resistance plateaus at the value of R_Ω (Fig. 4C-D). Regardless of the cell design or electrochemical technique, it is unavoidable that appreciable ohmic resistance will be included in the measurement. From these observations, it can be concluded that minimizing the ohmic resistance of the cell is critically important for obtaining accurate kinetic measurements at high current densities. Furthermore, ohmic resistance must always be quantitatively accounted for in the methods for data analysis. Ideally, R_Ω should be precisely measured, for example by PEIS, to allow for quantitative IR correction. If this is not feasible, then Eqs. 32-34 can also be used to

fit the value of R_Ω as an independent parameter; however, we have found that the accuracy of this approach is limited except when $R_{ct}^0 \gg R_\Omega$.
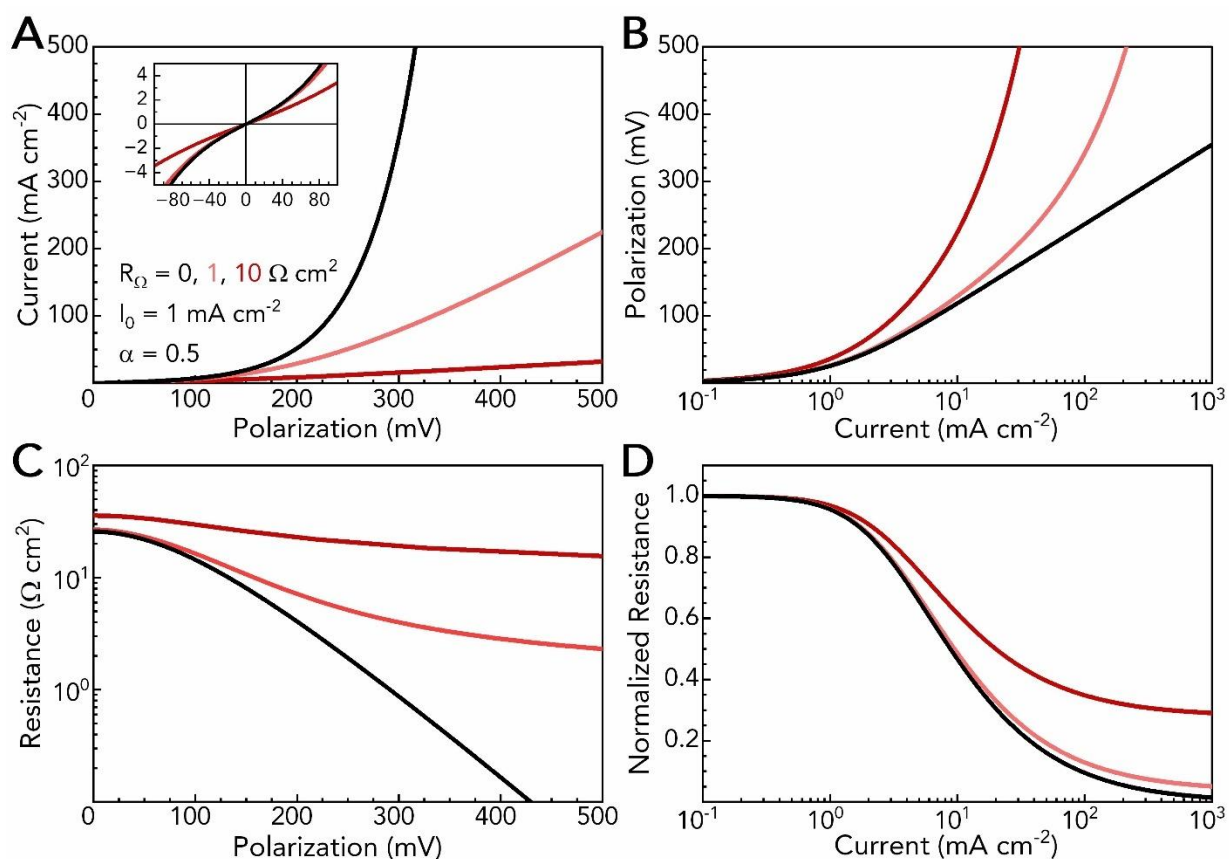

Figure 4. Effects of ohmic resistance on high-current kinetic measurements.
Mathematical model of polarization for symmetric Butler-Volmer kinetics, including ohmic resistance, showing **(A)** current versus polarization, **(B)** polarization versus current with a logarithmic scale (Tafel plot), (**C**) resistance versus polarization, and (**D**) normalized resistance versus current. Calculations were performed with $\alpha = 0.5$, $I_0 = 1$ mA cm^{-2}, and ohmic resistance (R_Ω) of 0, 1, or 10 Ω cm^2.

3.6. Electrochemical Measurement Techniques

There are several electrochemical techniques which can be used to measure the interfacial charge-transfer resistance of LIB AMs at high current densities. These techniques can be separated into three general classes: those which use direct current (*i.e.*, chronopotentiometry), those which use alternating current (*i.e.*, EIS), and those which use a superposition of the two (*i.e.*, operando EIS). In this work, we employ four electrochemical techniques: PEIS, S3E-CP, LA-GEIS, O-GEIS. A general overview of each electrochemical technique is provided in the following section.

PEIS is used to measure R_{ct}^0 by applying a small amplitude voltage perturbation about the equilibrium voltage of the cell [11]. The voltage perturbation should generally be limited to $5-25$ mV to maintain linearity of the impedance response [27]. The interfacial charge-transfer resistance manifests as a semi-circle in the Nyquist plot, and the value of R_{ct}^0 can be calculated through conventional techniques, such as equivalent-circuit analysis or other graphical methods. PEIS provides two main utilities in the context of high current density electrochemical measurements. First, PEIS provides a simple and rapid assessment of whether the kinetics are stable with time. PEIS should be conducted intermittently during measurements to detect any changes in R_{ct}^0 with time due to, for example, resistive heating or irreversible impedance growth. Secondly, while the values of α and I_0 cannot be independently measured with PEIS, the direct measurement of R_{ct}^0 constrains the possible values of α and I_0 based on Eq. 7. Specifically, by using the dimensionless notations for R_{ct} and R_{ct}' given, respectively, by Eqs. 13 and 21, α can be eliminated as an independent variable and the kinetics can be fully described in terms of R_{ct}^0 and I_0. This allows for accurate analysis even for truncated datasets, which do not include significant data within the linear region. For these reasons, PEIS should always be conducted alongside the other methods for kinetic measurements at high current densities.

26

The S3E methodology effectively eliminates the intrinsic non-stationarity of direct current measurements, as is discussed in detail in our previous work [18]. Briefly, the S3E-CP method consists of applying a series of short galvanostatic pulses across a wide range of current densities, while cycling the cell back to the same initial condition between each pulse. To approximate steady-state conditions, the voltage versus capacity data for each current pulse is extrapolated to a capacity of zero, yielding a dataset of voltage versus current. The overpotential is calculated by a subtraction of the IR drop, and the BV kinetic parameters can be fitted from the overpotential versus current data. S3E-CP measurements provide only the apparent electrode-level kinetic response, and unlike EIS, cannot directly deconvolute the contributions of multiple resistive processes within the electrode. Specifically, when $R_{ct} \approx R_p$, a non-uniform current distribution can occur within the porous electrode at high current densities, which is generally expected to preclude accurate measurement of the BV kinetic parameters [1,29]. Accurate S3E-CP measurements of α and I_0 can be obtained in the limiting case of $R_{ct} \gg R_p$, where the current distribution is uniform at high current densities; this condition can often be achieved with thin electrodes. However, there is also a limiting case in which $R_{ct} \ll R_p$ (*i.e.*, R_{ct} is immeasurably small and cannot be detected by EIS). In this case, the current distribution becomes semi-infinite at high current densities, resulting in a "double Tafel slope" behavior: this allows for an indirect measurement of the apparent α value of the AM [1,18].

LA-GEIS measurements are conducted by applying a large-amplitude sinusoidal current perturbation about the equilibrium voltage of the cell. To measure R_{ct} as a function of current, it is vital to use a current excitation instead of a voltage excitation, otherwise the effective current excitation would become frequency dependent [26]. When the current excitation amplitude (I^*) is high enough to enter the non-linear region of the kinetics (*i.e.*, $I^* \approx I_0$), a non-linear voltage

27

response to the sinusoidal current perturbation is generated, which manifests in two ways [30–32]. First, according to Eq. 13, the interfacial impedance should decrease with increasing current excitation amplitude, so the values of α and I_0 can – in theory – be calculated by simply fitting the R_{ct} versus current data to the reformulated BV equation. However, the non-linear voltage response also generates harmonic distortions of the impedance signal, which overestimate the magnitude of the linear impedance. When this harmonic distortion is significant, typical methods for EIS data analysis which assume the condition of linearity will give inaccurate results [33,34]. However, linearity of the impedance signal can be maintained if the analysis is limited to the weakly non-linear region of the kinetics where the harmonic distortion is sufficiently low.

O-GEIS measurements are conducted by applying a small-amplitude sinusoidal current excitation, which is superimposed about a large applied direct current. The applied current serves to bias the kinetics into the non-linear region, but does not directly contribute to the impedance measurement; the impedance is calculated only from the sinusoidal voltage response to the current excitation, and O-GEIS therefore measures the differential charge-transfer resistance (R'_{ct}) [28,34]. With a small amplitude current excitation (*i.e.*, 10% of the applied current), the impedance response is sufficiently linear even when the direct current bias is well within the non-linear region of the kinetics. O-GEIS can allow an independent measurement of the anodic and cathodic kinetics, since the applied current can be either positive or negative, however such measurements would require three-electrode cells. Unfortunately, it is challenging to maintain stationarity at both high current density and low frequency, which generally limits O-GEIS measurements to lower current densities than the other techniques.

28

4. Experimental Results

As discussed in detail in our previous work, it is highly challenging to obtain accurate electrochemical kinetic measurements of LIB AMs at high current densities [18]. Several necessary conditions must be maintained to ensure the accuracy of the measurements and data analysis. First, the AM, electrode, and cell designs must be optimized to eliminate any extraneous resistances or other artifacts in the data. Second, the ohmic resistance must be precisely measured and quantitively accounted for in the data analysis. Third, the condition of stability must be maintained: the kinetics of the system must be time-invariant and cannot change appreciably during or because of the kinetic measurements. Finally, for EIS measurements, the conditions of stationarity and linearity must be maintained to ensure validity of the data analysis. In the following section, it is quantitatively shown how each of these conditions can be satisfactorily met for S3E-CP, LA-GEIS, and O-GEIS measurements by optimizing the measurement methodology.

4.1. Active Material, Electrode, and Electrolyte Design

Regardless of the specific measurement method, it is critical to ensure that the AM, electrode, and cell design is optimized to eliminate any extraneous resistances or other artifacts, which could undermine the accuracy of the measurements. R_{ct} is inversely proportional to the electrode loading, while R_p is directly proportional to electrode loading [22,35,36]. Generally, the electrodes and separator should be as thin as possible, and the electrolyte should be as conductive as possible, to ensure that $R_{ct} \gg R_p$. LiCoO$_2$ (LCO) was synthesized with a narrow particle size distribution of ~ 1-5 µm by employing 0.5% Ti as a dopant to control crystal growth, allowing high-quality electrodes to be fabricated with a thickness of ~ 3 µm and a coat weight of ~ 1.3 mg cm^{-2} [37]. Notably, the single-crystal morphology is favorable to prevent particle cracking at high voltages, as this leads to changes in electrochemical surface area [38,39]. The electronic resistance of the

29

electrodes, and particularly contact resistance with the current collector, must be completely eliminated to obtain the most accurate measurements. This typically requires calendaring the electrode at high pressures, using a carbon-coated aluminum current collector, and maintaining high stack pressure during testing, but usually does not require large amounts of conductive carbon [40–42]. Contact resistance, like pore resistance, can be easily measured with PEIS of symmetric cells under blocking conditions [22]. Other than the low loading, the properties of the electrodes used in this work are comparable to those used in commercial cells; the LCO electrodes contain 97.5 wt% AM, are calendared to a density of 4.0 g cm^{-3} (~ 20% porosity), and show no measurable contact resistance.

It is also critical to avoid degradation (*i.e.*, impedance growth or capacity loss) of the AM during high-current measurements, which can expose the AM surface to extreme voltages. Given the notorious surface instability of LCO, both the AM and electrolyte were optimized to reduce surface reactivity [43]. The LCO is doped with 2% Al, 0.5% Ti, and 0.5% Mg to suppress deleterious phase transitions and oxygen loss at the surface [37]. The electrolyte uses FEC and LiPO$_2$F$_2$ additives to form passivation layers on the LCO surface, while the LiTDI additive inhibits chemical degradation of the electrolyte and subsequent reaction of acidic species with the LCO surface [6,44,45]. Without LiTDI, severe impedance growth occurs in LCO symmetric cells over a timescale of several hours, making it impossible to obtain accurate measurements (Fig. 6A). With 0.1M LiTDI, the impedance growth is much less severe (1% increase every ~ 6 h) and is highly linear with time, regardless of whether high-current measurements are conducted. Severe impedance growth of LCO symmetric cells has been observed previously, and is likely caused by chemical reactions of the AM surface with protic impurities in the electrolyte (*e.g.*, H$_2$O, HF), which may otherwise be consumed at the anode in half or full cells [46,47]. The kinetic

30

measurements conducted in this work generally require many data points collected across a wide range of current density and/or frequency, and each dataset takes several hours to collect. To mitigate the effects of this time-dependent impedance growth, the measurement conditions for each technique were optimized to reduce the total measurement time to < 5 h, ensuring a < 1% change in impedance over the course of the measurement. However, the irreversible impedance growth still leads to minor differences in the I_0 value measured between the different techniques, since the datasets were collected sequentially for the same cells.

4.2. Cell Design

Since the electrochemical data necessarily contain contributions from each component of the cell, it must be ensured that the measured voltage or impedance can be fully attributed to the working electrode (WE) [9,10,48]. Several different cell designs can be used for kinetic measurements, including half cells, full cells, 3-electrode cells, or symmetric cells. It must be emphasized that it very rarely appropriate to use a two-electrode half cell with a Li-metal counter electrode (CE) for interfacial kinetic measurements, since the impedance of the Li-metal CE is typically large and unstable in conventional electrolytes. The Li-metal CE can completely obscure the impedance spectrum of the WE during EIS, and cause an appreciable polarization during DC measurements [18,49]. For DC measurements, the use of a reference electrode (RE) in a 3-electrode cell can eliminate the polarization of the CE, but Li-metal is still a poor choice for CE since it is prone to degradation at high current densities. In a 3-electrode cell, Li-metal is typically an unsuitable CE for EIS measurements, since the impedance of the WE is distorted when the CE impedance is higher than the WE impedance [51-53]. We have found that LiFePO$_4$ and Li$_4$Ti$_5$O$_{12}$ are ideal CEs, while Morasch *et al.* have shown that free-standing Graphite on Li-metal is a suitable CE [18,50]. However, even if the CE impedance is sufficiently low, impedance distortions can

31

arise from the RE due to geometrical asymmetry of the cell, or stray capacitance/inductance or the RE [51–53]. Morasch *et al.* have also shown that these RE impedance artifacts can be eliminated with a gold wire micro RE in a Swagelok T cell, allowing accurate deconvolution of WE and CE impedance [50,54,55]. Unfortunately, this cell design requires a very thick separator which may make it unsuitable for direct-current measurements at high current density; however, this may not be problematic for LA-GEIS or O-GEIS measurements. The main disadvantage of 3-electrode measurements is that they generally require expensive custom-made cells that are delicate and tedious to assemble, which both limits experimental throughput and makes these measurements inaccessible for many researchers.

To make the electrochemical methods developed in this work widely accessible, we demonstrate that high-quality kinetic measurements can be obtained using only symmetric coin cells. Symmetric cells are ideal for the most precise EIS measurements; since there are two WEs, there are no artifacts or distortions which can arise from the CE or RE [10,48,56]. There is also little ambiguity in the data analysis: the WE impedance is simply half of the cell impedance. The main disadvantage of symmetric cells is that they, by definition, cannot determine the symmetry of the kinetics between the anodic and cathode directions; 3-electrode cells are generally needed for this purpose. Symmetric cells can be assembled by electrochemically pre-cycling two identical electrodes versus any CE (*e.g.*, Li-metal) to the desired SOC, then extracting and rinsing the electrodes, and building them into a coin cell with fresh electrolyte. Although somewhat tedious, this process is simple and reproducible and allows for rapid parallel testing. Advantageously, due to their sloping voltage profile, LCO symmetric cells can be quickly reset to the same SOC between each measurement by a short constant voltage hold at 0 V.

4.3. Measuring Ohmic Resistance for IR Correction

Accurate measurements of R_{ct} require quantitatively accounting for the ohmic resistance of the cell, particularly the pore resistance (R_p) of the electrodes. R_p can be measured with PEIS of symmetric cells under blocking conditions, which use the same electrolyte as for intercalating conditions, but are assembled with pristine electrodes [22]. This approach requires careful control of the electrode coating and cell building process to ensure that the coat weights of the electrodes are nearly identical (e.*g.*, < 2% different) between separate cells. The solution resistance (R_s) for both cells is determined by a linear interpolation of the high-frequency (HF) intercept of the impedance spectra. The low-frequency (LF) intercept under blocking conditions is calculated by a linear extrapolation of LF impedance data to $Z_{Im} = 0$ (Fig. 5A-B). The difference between the HF and LF intercepts is equal to one third of the pore resistance ($R_p/3$) [22]. The total ohmic resistance (R_Ω) under intercalating conditions is the sum of the solution resistance and pore resistance. Notably, there is a difference in the magnitude of the measured ohmic resistance between EIS and direct-current (DC) methods; for EIS measurements, $R_\Omega = R_s + R_p/3$, while for DC measurements, $R_\Omega = R_s + R_p$.

Once the value of R_Ω is measured, the value of R_{ct} can be calculated from the impedance spectra using either equivalent-circuit analysis or graphical methods. Since the symmetric cell contains two WEs, the measured value of R_{ct} is divided by two to give the contribution of a single electrode (Fig. 5C). For equivalent-circuit analysis, the PEIS spectra are fitted to a circuit of $Z = R_\Omega + R_{ct}/Q$, with the value of R_Ω determined from PEIS (Fig. 5D). Alternatively, Morasch's method can be used to calculate R_{ct} by subtracting the measured ohmic resistance from the real impedance value at the touchdown point of the semicircle [22]. A more precise measurement of R_{ct} can be obtained with this method by a quadratic interpolation of the Nyquist data near the

33

touchdown point (Fig. 5E). Specifically, the data point nearest the touchdown point is identified by finding the minimum value of dZ_{Im}/dZ_{Re}, then a quadratic equation is fit to the 7 data points centered around this point, and the root of the quadratic equation gives the interpolated Z_{Re} value of the touchdown point. This graphical method requires fewer data points than equivalent circuit fitting, which can reduce the total measurement time. This graphical method is also advantageous because the data analysis is simpler to automate and involves less subjectivity in selecting the data range for fitting. However, the touchdown point interpolation method may only give accurate results for very well-resolved semicircles, and therefore may not be suitable for many systems.
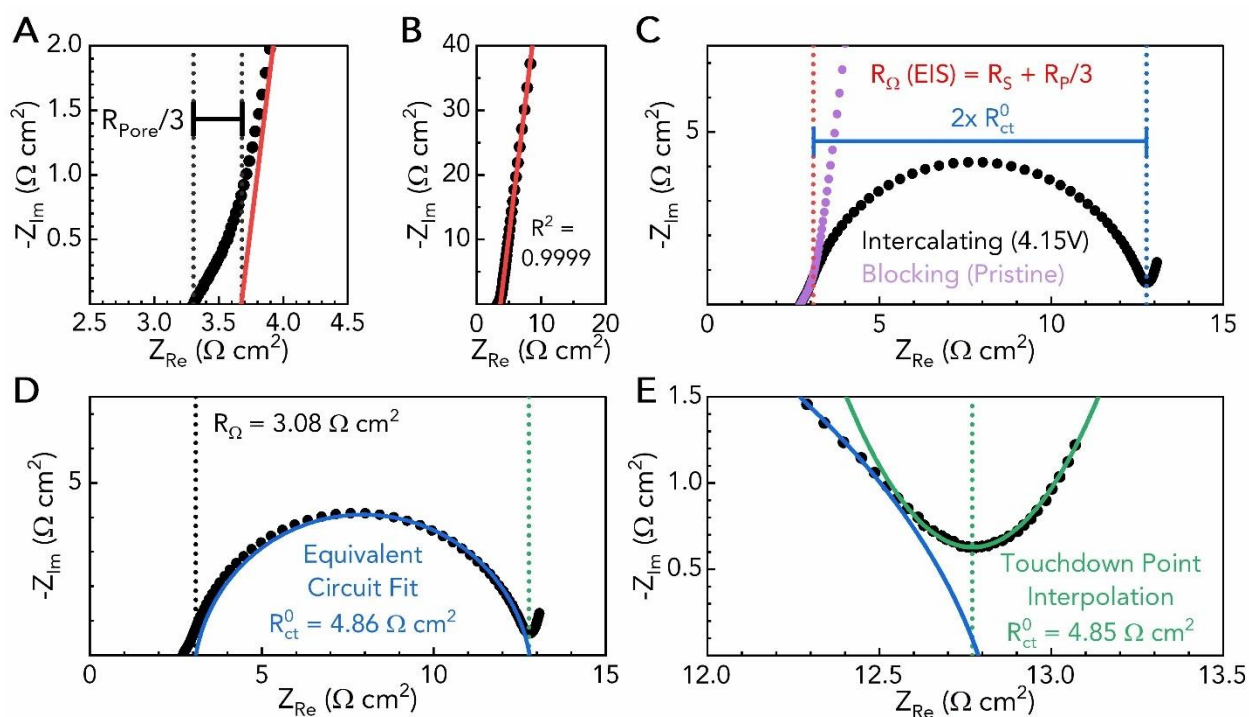

Figure 5. Deconvolution of ohmic and charge-transfer resistances with PEIS.
(A-B) Impedance spectrum of an LCO symmetric cell with pristine electrodes (blocking condition) between a frequency range of 500 kHz and 10 Hz, showing how the pore resistance (R_p) is calculated by linear extrapolation of the Nyquist data between a frequency of $250 - 2500$ Hz. **(C)** Impedance spectrum of an LCO symmetric cell with electrodes charged to 4.15 V vs. Li/Li$^+$ (intercalating condition) between a frequency range of 500 kHz and 1 Hz, compared to the spectrum blocking conditions, which is adjusted for the high-frequency intercept to improve comparability. **(D-E)** Comparison of results for the quantification of charge-transfer resistance from the PEIS spectrum by **(D)** equivalent-circuit modeling with a circuit of $Z = R_\Omega + R_{ct}/Q$, and by **(E)** quadratic interpolation of the touchdown point of the semicircle.

4.4. Stability

Besides irreversible resistance changes caused by AM or electrolyte degradation, there can also be reversible resistance changes, particularly due to changes in temperature. From the PEIS measurements of an LCO symmetric cell at different temperatures from 0 to 30 °C, the activation for the interfacial charger-transfer reaction was calculated from the Arrhenius equation to be 54.8 kJ mol^{-1} (Fig. 6B-C). At 25 °C, a 0.1°C or 1.0°C increase in temperature will therefore cause, respectively, a 0.7% or 7.0% decrease in the measured interfacial resistance. Consequently, very precise temperature control ($\pm < 0.1$°C) with an environmental chamber is required to ensure the accuracy and comparability of the measurements. More importantly, even very slight resistive heating, which can occur during high-current measurements, significantly affects the measured resistance. The otherwise stationary nature of LA-GEIS enables the use of very high current excitations, making it the most affected by resistive heating. Fig. 6D shows the first PEIS spectra collected immediately after a single-point LA-GEIS measurement at 1Hz with different excitation currents, while Fig. 6E shows the impedance versus time measured with PEIS every ~ 15 seconds afterwards. At an excitation of below 25 mA cm^{-2}, the resistive heating is negligible, while at 100 mA cm^{-2}, the measurement causes a 4% decrease in impedance. At very high current densities, and especially at low frequencies, the resistive heating becomes so severe that not even a single impedance point can be collected without temperature changes affecting the accuracy of the measurement [57]. Ideally, the impedance change due to resistive heating should be limited to < 1%, which under these conditions limits the maximum excitation current to ~ 50 mA cm^{-2}.

Resistive heating can be minimized by reducing the number of data points needed for analysis, so the touchdown point interpolation method was used to calculate R_{ct} for LA-GEIS measurements. Fig. 6F shows the impedance versus time during relaxation after collecting a LA-

35

GEIS spectrum between $1 - 10$ Hz with different excitation currents. The heating is more severe than for single-point measurements, but an excitation of up to 25 mA cm^{-2} can be achieved while limiting the reversible impedance change to $< 1\%$. When collecting the LA-GEIS datasets at multiple current densities, it is also necessary to allow the cell to fully relax between each measurement, otherwise the small temperature changes from each scan will add up. To mitigate resistive heating, the required rest time between measurements was determined as a function of current for each technique, and ranged from 2 to 30 min. Since the severity of resistive heating will be strongly dependent on both the magnitude of resistance and thermal properties of the cell, the maximum current and required rest times will need to be optimized for each specific system and electrochemical technique.

For O-GEIS, the resistive heating is not a significant factor limiting the data accuracy or maximum achievable current density. For S3E-CP measurements, the effect of heat generation within each current pulse is already inherently accounted for by the pseudo-steady-state extrapolation methodology [18]. However, when collecting a S3E-CP dataset, the resistive heating will affect each consecutive pulse unless the rest time between pulses is sufficient for full relaxation. The resistive heating is less severe for S3E-CP, for which the measurement time is inversely proportional to current, than for LA-GEIS, for which the measurement time is constant. The effects of resistive heating on total measurement time are also not as problematic for S3E-CP as for LA-GEIS, because only one measurement is needed per current. Overall, S3E-CP measurements can be conducted at much higher current densities than the other methods developed in this work. For example, satisfactory data were collected at a current density of up to 250 mA cm^{-2} with a 1 h rest time between pulses, but this leads to long measurement times.

https://doi.org/10.26434/chemrxiv-2024-hndjp **ORCID:** https://orcid.org/0000-0002-0257-3086 Content not peer-reviewed by ChemRxiv. **License:** CC BY 4.0
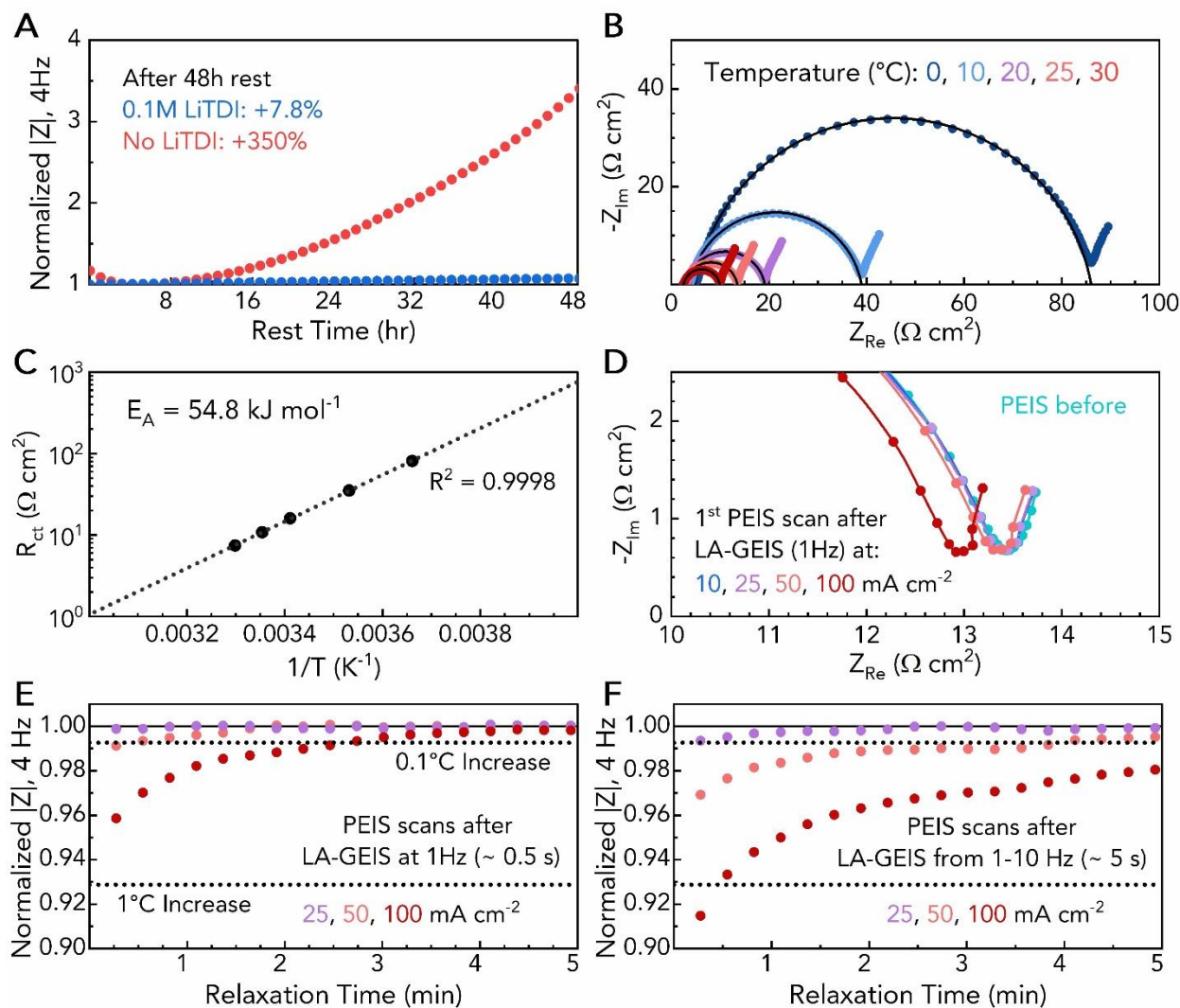
Figure 6. Maintaining stability during repeated high-current kinetic measurements.
(A) Normalized impedance magnitude (|Z|) at 4 Hz versus rest time measured with PEIS for LCO symmetric cells at 50% state-of-charge, with an electrolyte containing 1.2 M $LiPF_6$ + 0.1 M $LiPO_2F_2$ in 25 : 75 w/w FEC : DMC, and with or without 0.1 M LiTDI. **(B)** Impedance spectra of an LCO symmetric cell measured with PEIS (500 kHz – 100 mHz) at various temperatures between 0 and 30°C, with equivalent-circuit fits to calculate the values of R_{ct}. **(C)** Plot of linearized charge-transfer resistance measured with PEIS versus inverse of temperature, with a best fit line to calculate the activation energy from the Arrhenius equation. **(D)** Impedance spectra of an LCO symmetric cell collected with PEIS (1 Hz – 10 kHz) immediately after single-frequency (1 Hz) LA-GEIS measurements with excitation amplitudes ranging from 10 to 100 mA cm^{-2}. **(E)** Normalized |Z| at 4Hz versus relaxation time after single-frequency LA-GEIS measurements (1 Hz, ~ 0.5 s per scan). **(F)** Normalized |Z| at 4 Hz versus relaxation time after multi-frequency LA-GEIS measurements (1 – 10 Hz, 10 points per decade, ~ 5 s per scan).

37

4.5. Stationarity

LA-GEIS is inherently stationary at relatively high frequencies (> 1 Hz), since large concentration or resistance changes do not have time to accumulate, and no net capacity change occurs due to the measurement. DC measurements (*e.g.*, chronopotentiometry) are inherently non-stationary: the cell voltage changes continuously during the measurement, due to the sloping OCV profile of LCO, as well as the resistance growth arising from concentration polarization of both the AM and electrolyte. However, stationary conditions for chronopotentiometry measurements can be easily approximated with a pseudo-steady-state extrapolation (S3E) approach [18]. This is because DC measurements allow rapid data acquisition times (*e.g.*, < 1 ms), so large amount of voltage versus capacity data can be collected before the resistance growth becomes severe, even at extreme current densities. A simple linear extrapolation of the voltage versus capacity data to a capacity of zero can give a remarkably accurate approximation of steady-state conditions (Fig. 7A).

O-GEIS measurements, like chronopotentiometry, are inherently non-stationary. Unfortunately, EIS data collection requires averaging the voltage data over at least one, and ideally many, excitation periods [11,28,34]. At low current densities and/or high frequencies, it can be possible to collect an entire O-GEIS spectrum without appreciable changes in the cell voltage. However, at high current densities and/or low frequencies, the cell voltage can change significantly even during the measurement of a single impedance point, which can lead to inaccurate results (Fig. 7A) [57,58]. For high-current O-GEIS measurements, the data should ideally be collected with a single impedance point per scan, and drift correction must be employed to compensate for changes in the cell voltage during the measurement of each impedance point. The process of drift correction can be visualized by subtracting the voltage versus time data of O-GEIS and S3E-CP

https://doi.org/10.26434/chemrxiv-2024-hndjp ORCID: https://orcid.org/0000-0002-0257-3086 Content not peer-reviewed by ChemRxiv. **License:** CC BY 4.0

measurements at the same applied current, revealing a highly linear sinusoidal voltage response to the O-GEIS excitation (Fig. 7B). The Biologic EC-Lab software has a built-in drift correction option, which accounts for changes in the cell voltage using a Fourier transform methodology. However, for the EC-Lab drift correction feature to perform well, many excitation periods must be averaged to avoid truncation errors when calculating the discrete Fourier transform.

The data acquisition time for a single impedance point is inversely proportional to frequency, while the total capacity for each O-GEIS measurement is directly proportional to both the acquisition time and current density. As a result, at both high current densities and low frequencies, very significant capacity changes (*e.g.*, > 10% SOC) can occur during the collection of a single impedance point, which leads to severe non-stationarity (Fig. 7C). The effectiveness of the Fourier transform method of drift correction is also hindered by the lower number of excitation periods which can be collected at low frequencies. Non-stationarity for O-GEIS measurements manifests as a severe distortion of the impedance spectrum at low frequencies (Fig. 7D) [59]. Stationarity can be quantitatively assessed with a Kramers-Kronig (KK) transformation of the impedance data, but unfortunately the KK transform is not suitable for truncated spectra, as are used in this work [57,60]. Alternatively, stationarity can be assessed based on the value of the non-stationary distortion (NSD), which is calculated from a discrete Fourier transform based on the magnitude of the impedance response (|Y|) at frequencies adjacent to the fundamental frequency (*f*), according to:

$$(35) \quad NSD = \frac{1}{|Y_f|} \sqrt{\left|Y_{f-\Delta f}\right|^2 + \left|Y_{f+\Delta f}\right|^2}$$

For O-GEIS measurements, the impedance spectrum starts to become visibly distorted once the NSD reaches ~ 10%, which occurs below a frequency of ~ 10 Hz (Fig. 7E). A conservative limit of 3% NSD was set, which limits the lower frequency to 100 Hz at 25 mA cm^{-2} applied current
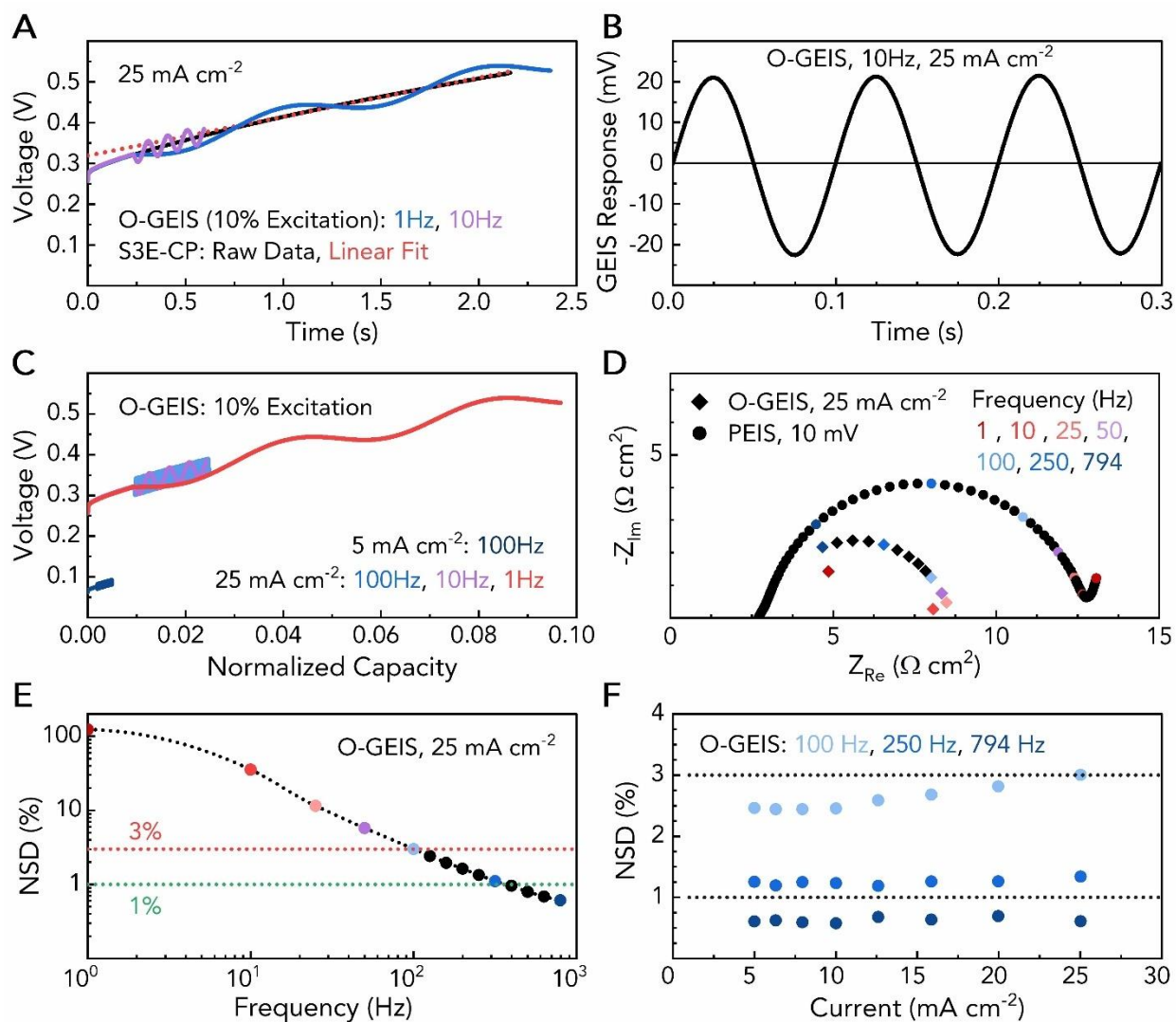
39

Figure 7. Maintaining stationarity during high-current O-GEIS measurements.
(A) Voltage versus time data from an S3E-CP measurement of an LCO symmetric cell at 25 mA cm^{-2} applied current, compared to O-GEIS measurements at the same applied current with an excitation of 2.5 mA cm^{-2} at a frequency of 1 Hz or 10 Hz. Data were recorded in a dual-channel configuration. **(B)** Voltage response to the sinusoidal current excitation calculated by subtracting the voltage versus time data from O-GEIS and S3E-CP measurements. **(C)** Voltage versus normalized capacity for O-GEIS measurements at applied currents of 5 or 25 mA cm^{-2} and frequencies of 1, 10, or 100 Hz. **(D)** Comparison of the impedance spectra for PEIS (500 kHz – 1 Hz, 10 mV excitation) and O-GEIS (794 Hz – 1 Hz) with a 25 mA cm^{-2} applied current and 2.5 mA cm^{-2} excitation. **(E)** Non-stationary distortion (NSD) versus frequency for O-GEIS measurements at 25 mA cm^{-2}, calculated with EC-Lab Quality Indicators. **(F)** NSD versus applied current for O-GEIS measurement at frequencies of 100, 250, and 794 Hz.

40

density. A frequency range of 100 – 794 Hz is still sufficient to fit half of the semicircle with equivalent-circuit analysis, and most of the data for each spectrum maintains NSD of < 2% (Fig. 7F). Overall, although non-stationarity restricts the lower frequency limit of O-GEIS measurements, satisfactory data to measure the interfacial kinetics can still be obtained at relatively high current densities.

4.6. Linearity

In the literature, it is widely stated that linearity is a necessary condition for accurate EIS measurements, but there are inconsistencies in terminology which should be clarified [11,26,61,62]. First, it must be emphasized that there is a fundamental difference between the linearity of the current versus overpotential relation (*i.e.*, the kinetics), and the linearity of the impedance signal (*i.e.*, the measurement). Additionally, the term "non-linearity" has been used in the literature to describe both kinetics for which the current versus overpotential relation is exponential, or for which the current versus overpotential relation is asymmetric between the anodic and cathodic directions. For clarity, we refer to the former case as non-linearity, and the latter case as asymmetry. Both non-linearity and asymmetry of the kinetics can, but do not necessarily, result in a non-linear impedance signal [30]. Likewise, it is possible for the impedance signal to contain significant non-linear contributions even if the kinetics are linear and symmetric [63]. To measure the interfacial kinetics with EIS at high current densities, it must therefore be ensured that the impedance signal is sufficiently linear even though measurements are conducted within the non-linear region of the kinetics.

There are many methods reported in the literature for assessing the linearity and symmetry of interfacial kinetics. For example, deviation from an elliptical response in the Lissajous (I vs.

41

V) plots provides qualitative evidence of non-linearity, while differences in current between the anodic and cathodic direction indicate asymmetry [61,64]. From LASV measurements of LCO symmetric cells, the kinetics appear to be highly non-linear, but almost perfectly symmetric (Fig. 8A). This non-linearity is also visible in the voltage versus time data from LA-GEIS measurements (Fig. 8B). A decrease in resistance with increasing excitation amplitude is viewed as a telltale sign of non-linear behavior during EIS measurements [27]. Indeed, the decrease in interfacial impedance with increasing excitation amplitude for LA-GEIS measurements is clear evidence of non-linear kinetics (Fig. 8C). In the literature, it has sometimes been stated that the EIS data are "corrupted" by this non-linearity, rendering the data invalid for methods of data analysis which assume linearity, such as equivalent circuit analysis [26,27,62]. On the contrary, this decrease in interfacial resistance is not an artifact or distortion of the impedance data; it is literally the physical manifestation of the non-linear current versus overpotential relationship. In fact, this decrease in interfacial resistance with increasing current is exactly the non-linearity which must be experimentally measured to fit the electrochemical data to the BV equation.

Unfortunately, for EIS measurements, the combined effects of non-linear kinetics and a large-amplitude excitation can result in harmonic distortions of the impedance signal, which complicate data analysis [32,33,61]. Specifically, modern potentiostats use a frequency response analyzer (FRA) to measure the impedance, which essentially works by taking a Fourier transform of the DC data to calculate the magnitude and phase shift of the impedance signal [28]. The FRA can separate the response at the fundamental frequency (*i.e.*, the linear response) from the responses at other frequencies. When the LA-GEIS current excitation amplitude is sufficiently large to reach the non-linear region of the kinetics, a series of voltage responses with decreasing amplitudes are also generated at integer multiples of fundamental frequency; these voltage

42

responses are referred to as the harmonics [30–33,62]. Although the FRA can separate the linear response from the harmonics, the magnitude of the linear response is still distorted by the harmonics, causing an overestimation of the measured linear impedance [33]. Qualitatively, these harmonic distortions manifest as a visible elongation of the semicircle at low frequency (Fig. 8C). The harmonics can be measured by calculating the discrete Fourier transform of the voltage versus time data from EIS, which is done automatically by many modern potentiostats (Fig. 8D-E). In the case of half-wave symmetry (*i.e.*, current-voltage relation is symmetric about the origin), only odd harmonics are generated; this condition is achieved by the physical symmetry of symmetric cells, even if the kinetics are asymmetric (Fig. 8D) [65]. At high excitation currents (*e.g.*, 100 mA cm^{-2}), the magnitude of the harmonics becomes quite significant relative to the linear response, and harmonic responses above the noise level can observed up to the 19th harmonic (Fig. 8E). Overall, measuring the interfacial kinetics at high current densities with EIS requires either quantitatively accounting for these harmonic distortions, or ensuring that they are negligible; in this work, the latter approach is taken because it is significantly simpler.

Several analysis techniques are available for assessing the linearity of EIS measurements, the most quantitative of which is to calculate the total harmonic distortion (THD), which is the ratio of the magnitudes of the harmonics relative to the fundamental frequency [61]. The THD, calculated up to the Nth harmonic, is given by:

(36) $THD_N = \frac{1}{|Y_1|}\sqrt{\sum_{n=2}^{N}|Y_n|^2}$

where $|Y_n|$ is the magnitude of the response signal at each harmonic frequency [33,61]. The THD versus frequency data, which is calculated up to 7th harmonic in the EC-LAB software, is shown for LA-GEIS measurements with different current excitations (Fig. 7F). THD is always low (< 1%) at high frequencies (*e.g.*, > 1 kHz) where ohmic resistance and double-layer capacitance,

43

which are both linear processes, dominate the voltage response [66]. For low excitation currents, THD remains small even at low frequencies because the interfacial kinetics are maintained within the linear region. For high excitation currents, THD increases sharply with decreasing frequency in the intermediate frequence range, where the voltage response shifts from mostly capacitive to mostly faradaic [66]. THD plateaus at low frequencies, and as a function of current, to values of ~ 10%. In general, a THD of < 1% is considered sufficiently linear, while a THD of > 3% can be considered problematic [61]. To ensure linearity conditions for LA-GEIS data analysis, the current range used to fit the kinetic data was limited to ~ 10 mA cm^{-2} RMS to maintain THD < 2%.

For O-GEIS measurements, the harmonic distortions are negligible. Due to the small-amplitude excitation (≤ 2.5 mA cm^{-2}), the amplitude of the sinusoidal voltage response is limited to < 25mV (Fig. 7B). Only the even harmonics are generated above the noise level, which arise from a slight asymmetry of the voltage response about the direct current bias due to the non-linear kinetics (Fig. 8G). THD for all O-GEIS measurements is maintained at <1%, which is considered exemplary (Fig. 8H) [61]. Notably, THD is sensitive to the excitation current, and there can be tradeoffs between reducing THD and increasing the signal-to-noise ratio. At low applied current densities, the excitation amplitude can be increased to ~ 25% of the applied current to achieve better signal-to-noise, while at high applied current densities, the excitation can be as low as < 5% while maintaining sufficient signal-to-noise. Overall, for either LA-GEIS measurements at relatively low current densities, or for O-GEIS measurements even at high current densities, the impedance signal is shown to be sufficiently linear for accurate EIS data analysis.
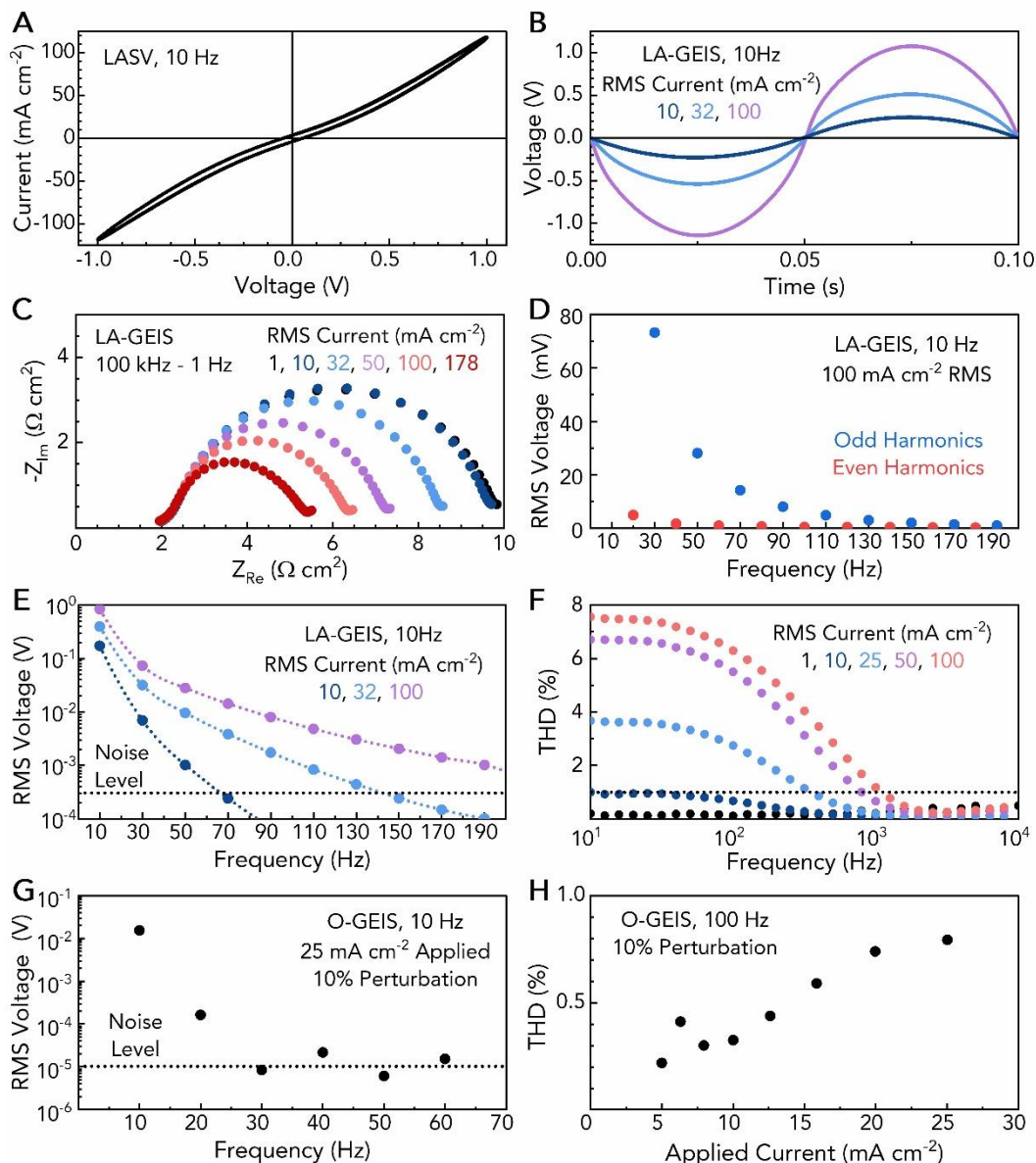
Figure 8. Maintaining linearity of the impedance response at high current densities.
(**A**) Current versus voltage data from large amplitude sinusoidal voltammetry (LASV) of an LCO symmetric cell between -1 V and 1 V at a frequency of 10 Hz. (**B**) Voltage versus time data collected in a dual-channel configuration for LA-GEIS measurements at 10 Hz with root-mean-square (RMS) current excitations of 10, 32, and 100 mA cm^{-2}. (**C**) Preliminary impedance spectra collected with single-point LA-GEIS measurements at frequencies of 100 kHz – 1 Hz with RMS current excitations of 1 – 178 mA cm^{-2}. (**D**) Magnitude of the voltage response as a function of frequency calculated by a direct Fourier transform of the voltage versus time data from LA-GEIS measurements at 10 Hz and 100 mA cm^{-2} RMS excitation. (**E**) Magnitude of the odd voltage harmonics as a function of frequency for LA-GEIS measurements at 10, 32, or 100 mA cm^{-2} RMS excitation. (**F**) Total Harmonic Distortion (THD) calculated up to the 7th harmonic versus frequency for LA-GEIS measurements with RMS excitations of 1 – 100 mA cm^{-2}. (**G**) Magnitude of the voltage harmonics from O-GEIS (10 Hz, 25 mA cm^{-2} applied current, 10% excitation) as a function of frequency, calculated by a direct Fourier transform of the voltage versus time data from Figure 7B. (**H**) THD versus applied current for O-GEIS measurements at 100 Hz with a 10% excitation.

45

4.7. S3E-CP Measurement Results

For the S3E-CP measurements, LCO symmetric cells at 50% SOC were subjected to galvanostatic pulses with current density ranging from 5 – 100 mA cm^{-2}. Each pulse was terminated at a capacity limit of 15 μAh cm^{-2}, which is ~ 10% of the cyclable capacity of the symmetric cell. Immediately after each pulse, the cell was held at an applied voltage of 0 V. This resulted in a peak current comparable to the galvanostatic pulse, and the current decayed to less than a C/100 rate within 3 min. The length of the rest step at 0 V was varied as a function of current (from 3 to 30 min) to reduce measurement time while mitigating resistive heating. After each rest step, a PEIS measurement was taken to ensure stability. The maximum current density was limited to 100 mA cm^{-2} to reduce the total measurement time. Before and after collecting the S3E-CP dataset, which took ~ 4 h, the impedance measured with PEIS increased by only 0.3% (Fig. 9A). For each current pulse, a linear fit was applied to the voltage versus capacity data in the range of 50 – 90% of the normalized capacity of the pulse, or a capacity of 7.5 – 13.5 μAh cm^{-2} (Fig. 9B). This capacity range was selected to maximize the average R^2 value of the best fit lines across the entire current range, which ranged from 0.9996 to > 0.9999. To obtain accurate data, the same capacity range should be used across the entire current range, and the optimal capacity range should be determined for each specific system. The minimum current density was limited to 5 mA cm^{-2} because it was found that the sloping voltage profile of LCO, unlike the flat voltage profile of LFP, caused inaccuracy of the extrapolated voltage at very low current densities [18].

The intercept of each best fit line at a capacity of zero yields the extrapolated pseudo-steady-state voltage for each applied current density. The measured polarization of the cell contains contributions from both the overpotential and the IR drop. The overpotential is calculated by subtracting the IR drop according to the value of ohmic resistance measured with PEIS, with R_Ω =

$R_s + R_p = 3.52\ \Omega\ \text{cm}^2$ (Fig. 9C). The appearance of a well-defined Tafel slope after IR correction indicates that the IR correction is successful (Fig. 9D). Nonetheless, the IR correction may be imperfect, which could lead to a slight inaccuracy of the measured values of α and I_0. The overpotential versus current data were fitted to both a one-step BV model (Eqs. 9 - 13) and a Tafel model (Eq. 14). The BV model yields $\alpha = 0.422$, $I_0 = 4.43\ \text{mA cm}^{-2}$, and $R_{ct}^0 = 6.87\ \Omega\ \text{cm}^2$. From the measured Tafel slope of 141 mV per decade, the Tafel model yields $\alpha = 0.418$ and $I_0 = 4.43$ mA cm^{-2}. Based on the agreement between the BV and Tafel models, it is likely that accurate S3E-CP results can be obtained from truncated datasets in either the weakly non-linear or Tafel regions of the kinetics. Surprisingly, the value of R_{ct}^0 measured with S3E-CP (6.87 $\Omega\ \text{cm}^2$) is higher than that measured with PEIS (4.84 $\Omega\ \text{cm}^2$) by a factor of 1.42, which is almost exactly equal to $\sqrt{2}$ (Fig. 9E). This translates to a proportionally lower measured I_0 value for DC than for EIS measurements, according to:

$$(37)\quad R_{ct}^0(DC) \approx \sqrt{2}\, R_{ct}^0(EIS)$$

$$(38)\quad I_0(EIS) \approx \sqrt{2}\, I_0(DC)$$

Despite this difference, the S3E-CP data perfectly fit the BV equation for a 1-step reaction with $\alpha \approx 0.42$, as shown by the agreement with the BV model in the dimensionless plot of normalized resistance versus normalized current (Fig. 9F).

4.8. LA-GEIS Measurement Results

For LA-GEIS measurements, a touchdown point interpolation method was used to calculate the magnitude of R_{ct} from the impedance spectra (Fig. 5). The current excitation ranged from 1 to 50 mA cm^{-2}, with 10 points per decade spacing in logarithmic spacing. At each current, the impedance spectrum was collected in a single scan with no averaging. Since the characteristic frequency of the semicircle increases as the resistance decreases, a variable frequency range was
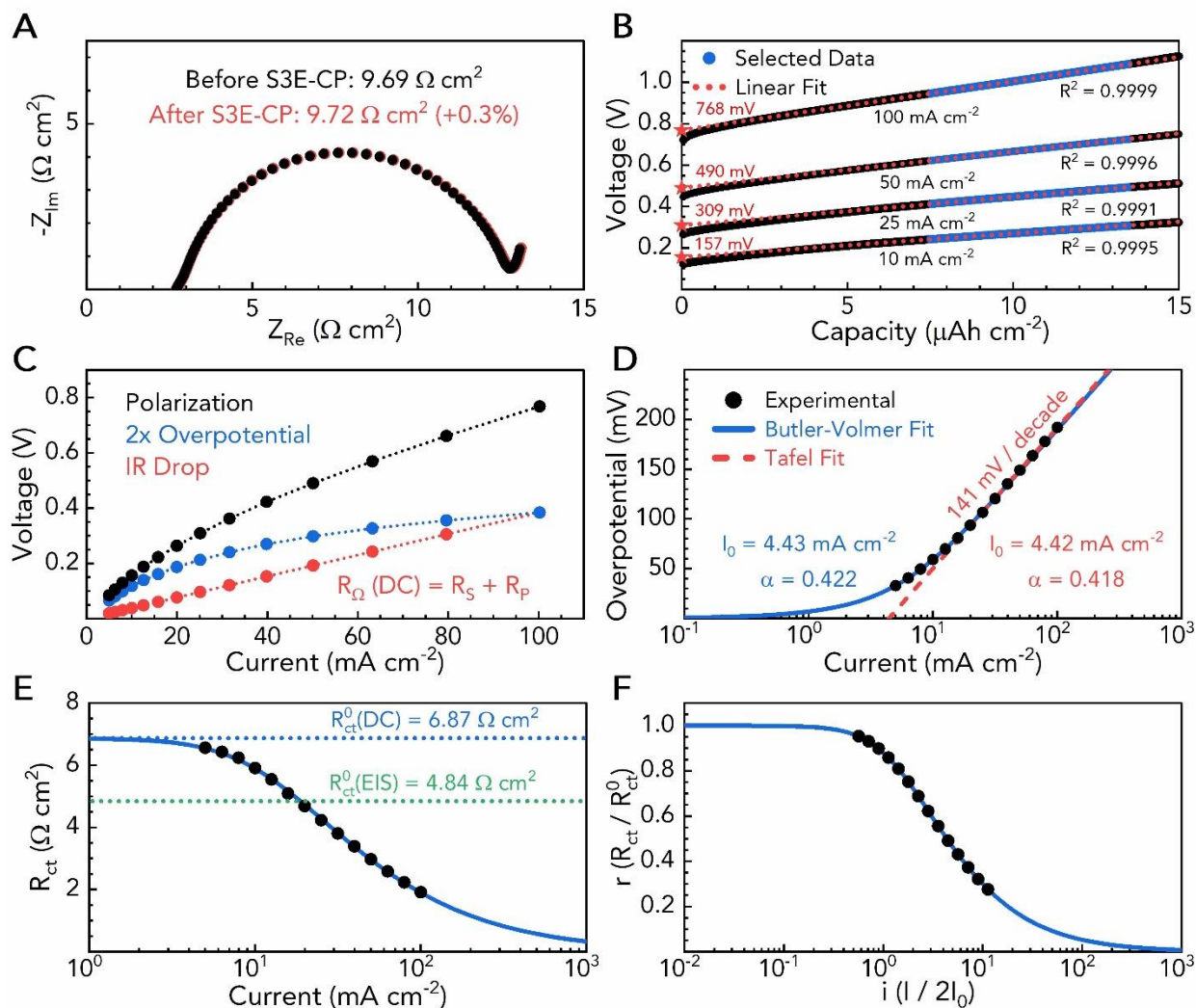
Figure 9. S3E-CP measurement results.
(A) PEIS spectra (500 kHz – 1 Hz) of an LCO symmetric cell collected before and after the S3E-CP measurements. **(B)** Raw voltage versus capacity data from S3E-CP pulses at current densities of 5 – 100 mA cm^{-2}, showing how a linear extrapolation from the selected data range is used to calculate the pseudo-steady-state voltage. **(C)** Steady-state voltage versus current data, showing how the overpotential is calculated by subtracting the IR drop from the measured polarization. **(D)** Overpotential versus current data from 5 to 100 mA cm^{-2}, with a BV Equation (Eq. 9) fit to calculate α and I_0 by least squares error minimization, and a linear fit to calculate α and I_0 from the Tafel Equation (Eq. 14). **(E)** Charge-transfer resistance (R_{ct}) versus current data with a BV model fit (Eq. 10), showing a 1.42x difference in the linearized charge-transfer resistance between S3E-CP and PEIS measurements. **(F)** Dimensionless plot of normalized charge-transfer resistance (r) versus normalized current (i), comparing the experimental data and BV model (Eq. 13).

48

used to resolve the touchdown point while minimizing the number of data points. The frequency range varied from 1 – 10 Hz at 1 mA cm^{-2} to 3 – 15 Hz at 50 mA cm^{-2}. The rest time between impedance scans ranged from 1 min at 1 mA cm^{-2} to 10 min at 50 mA cm^{-2}. PEIS spectra were collected after each rest step to ensure stability. Before and after collecting the LA-GEIS dataset, which took ~ 2 h, the impedance measured with PEIS decreased by 0.4% (Fig. 10A) due to slight resistive heating.

The raw impedance data for the LA-GEIS measurements are shown in Fig. 10B, while the interpolated touchdown points are shown in Fig. 10C. Two factors must be accounted for to accurately fit the LA-GEIS data to the BV model. First, the RMS current, not the current excitation amplitude, must be used to fit the R_{ct} versus current data; otherwise, α will be underestimated by a factor of $\sqrt{2}$ and I_0 will be overestimated by a factor of $\sqrt{2}$. Second, it must be ensured that the harmonic distortion of the impedance signal is sufficiently low to satisfy the condition of linearity. With an upper limit of 2% THD, the maximum RMS current for fitting the LA-GEIS data is limited to ~ 10 mA cm^{-2}, which corresponds to a normalized current ($i = I/2I_0$) of ~ 1. Generally, the current range of $0.1 < i < 1$ seems to be ideal for accurate analysis of the LA-GEIS data. Within this current range, the measured R_{ct} decreases by ~ 12%, which is sufficient to fit the experimental data. (Fig. 10D). The normalized resistance ($r = R_{ct}/R_{ct}^0$) versus normalized current data were fitted to Eq. 13 with least squares error minimization to calculate the value of I_0, and the value of α was calculated from Eq. 7. Within the optimal RMS current range of $< ~ 10$ mA cm^{-2}, the LA-GEIS measurements yield $\alpha = 0.431$ and $I_0 = 6.11$ mA cm^{-2}. If the LA-GEIS data at high current density are used to fit the BV model, the value of α is underestimated due to harmonic distortions, however this leads to only a relatively small inaccuracy. For example, $\alpha = 0.438$ is calculated for
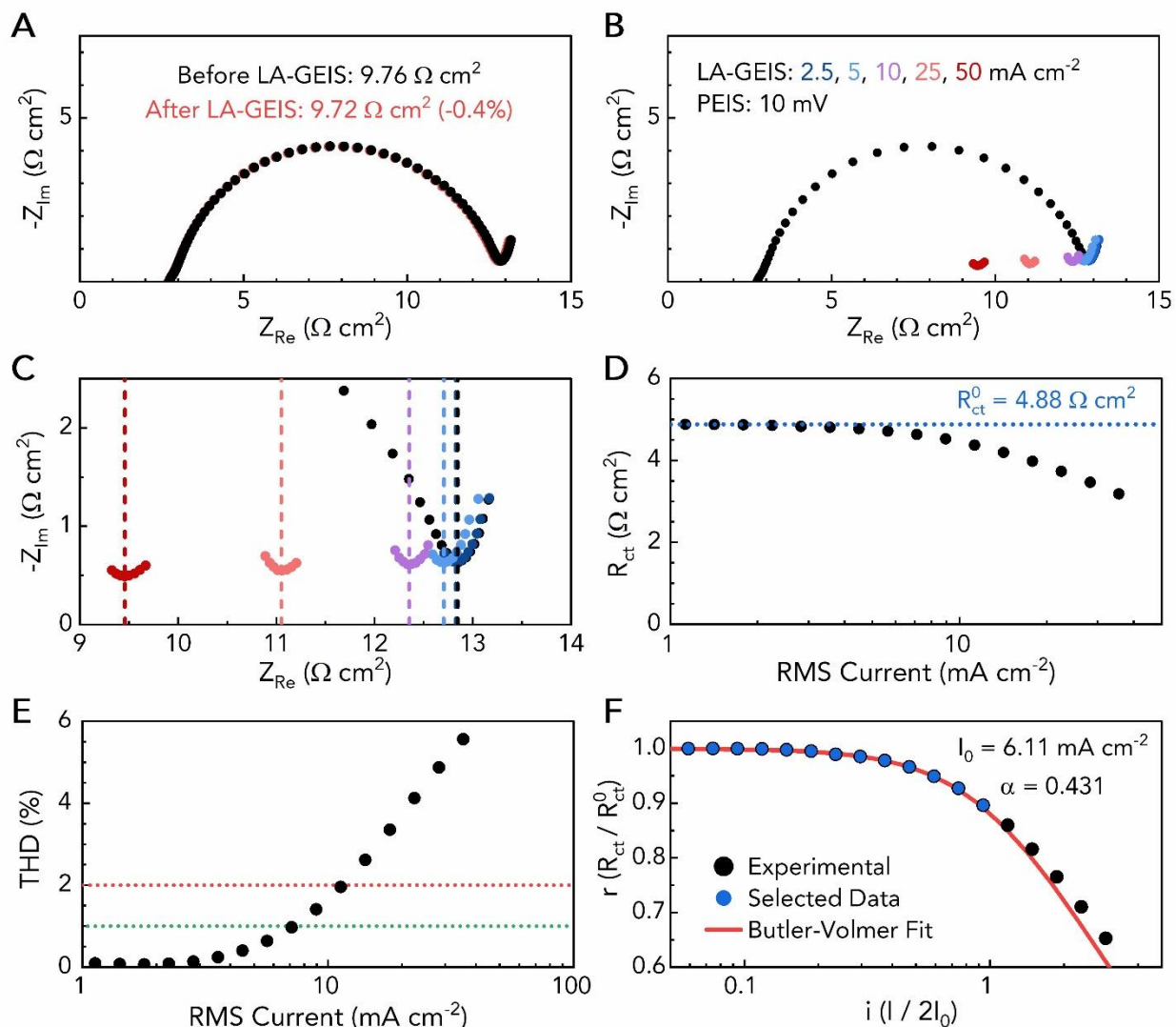
49

Figure 10. LA-GEIS measurement results.
(A) PEIS spectra (500 kHz – 1 Hz) of an LCO symmetric cell collected before and after the LA-GEIS measurements. **(B-C)** Nyquist plots of the raw impedance data collected from PEIS (500 kHz – 1 Hz) and LA-GEIS (1 – 15 Hz) with excitation currents of 2.5 – 50 mA cm^{-2}, showing the interpolated touchdown points of the semicircles. **(D)** Charge-transfer resistance (R_{ct}) versus root-mean-square (RMS) current data calculated by subtracting the real impedance at the touchdown points by the ohmic resistance measured with PEIS. **(E)** Total harmonic distortion (THD) versus RMS current for LA-GEIS measurements at 1 Hz. **(F)** Normalized charge-transfer resistance (r) versus normalized current (i) data, with a BV model fit (Eq. 13) to the current range of $i < 1$, where THD < 2%.

50

data with RMS excitation currents of $< \sim 5$ mA cm^{-2}, while $\alpha = 0.409$ is calculated for data with

RMS excitation currents of $< \sim 25$ mA cm^{-2}. The α value agrees extremely well between S3E-CP

and LA-GEIS measurements, and the value of R_{ct}^0 agrees perfectly between LA-GEIS and PEIS

measurements. However, the values of R_{ct}^0 and I_0 from PEIS and LA-GEIS both differ by a factor

of $\sqrt{2}$ from those measured with S3E-CP.

4.9. O-GEIS Measurement Results

O-GEIS measurements were conducted between the frequency range of $100 - 794$ Hz, with

an applied current density ranging from 5 to 25 mA cm^{-2}, and a current excitation of 10% of the

applied current ($0.5 - 2.5$ mA cm^{-2}). The maximum current and minimum frequency were limited

to ensure stationarity, and NSD of $< 3\%$ was maintained for all measurements. The data were

collected with a single impedance point per scan with no averaging, and with the EC-Lab drift

correction feature enabled. Between each scan, the cell was held at 0 V applied voltage for rest

times ranging from 2 min at 5 mA cm^{-2} to 5 min at 25 mA cm^{-2}. PEIS spectra were collected

between each current density to ensure stability. Before and after collecting the O-GEIS dataset,

which took ~ 3 h, the impedance measured with PEIS increased by 0.6% (Figure 11A). The raw

impedance data for the entire dataset is shown in Fig. 11B. The differential charge-transfer

resistance (R_{ct}') at each applied current is quantified by fitting each impedance spectrum to an

equivalent-circuit model of $Z = R_\Omega + R_{ct}/Q$, with the value of R_Ω measured with PEIS (Fig. 11C).

The capacitance (2.9 mF s) and phase angle (0.89) of the constant phase element (Q) are nearly

identical between PEIS and O-GEIS measurements and are consistent with values reported in the

literature [39].

Since O-GEIS combines an impedance measurement with an applied DC bias, the empirical

$\sqrt{2}$ difference in the magnitude of I_0 measured between EIS and DC techniques must be

51

quantitatively accounted for in the data analysis. Specifically, to obtain α values from O-GEIS which are consistent with the other measurement techniques, the expressions for differential charge-transfer resistance must be modified by a factor of $\sqrt{2}$ according to:

(39) $R'_{ct} = \left(\frac{RT}{2\alpha F I_0}\right)\left(1 + \left(\frac{I}{2\sqrt{2}\,I_0}\right)^2\right)^{-\frac{1}{2}}$

(40) $r' = \left(1 + \frac{i^2}{2}\right)^{-\frac{1}{2}}$

If this modification is not made, then the data are still equally consistent with the BV equation, but the calculated values of α and I_0 disagree with the other techniques: α is underestimated by a factor of $\sqrt{2}$, and I_0 is overestimated by a factor of $\sqrt{2}$. This is the same error that occurs for LA-GEIS measurements if the current is not calculated on an RMS basis. Counterintuitively, it seems that the applied DC bias must be treated on an RMS basis for the O-GEIS data analysis.

The experimental R'_{ct} versus current data fit the one-step BV model reasonably well, yielding $\alpha = 0.460$, $I_0 = 5.79$ mA cm^{-2}, and $R^0_{ct} = 4.82$ Ω cm^2 (Fig. 11D). The value of I_0 from O-GEIS is higher than from S3E-CP by a factor of $\sim \sqrt{2}$, similarly to LA-GEIS. The measured α value of 0.460 from O-GEIS also differs slightly from the values obtained from S3E-CP (0.420) and LA-GEIS (0.431) measurements, which agree more closely with each other. Upon close inspection of the normalized resistance versus current plots, the BV model for a one-step reaction does not fit the O-GEIS data well within the intermediate current range: the resistance decreases more quickly than expected at low current densities, but more slowly than expected at high current densities (Fig. 11E). This indicates the possibility of a multi-step reaction, as shown by Fig. 3. At either very low or very high current density, a two-step reaction with $\alpha_1 = 0.5$ and $\alpha_2 = 3$ is predicted to behave as a one-step reaction with an apparent α value of 0.429. The values of $\alpha = 0.42$ obtained from S3E-CP measurements at high current densities, and $\alpha = 0.43$ obtained from LA-GEIS at low
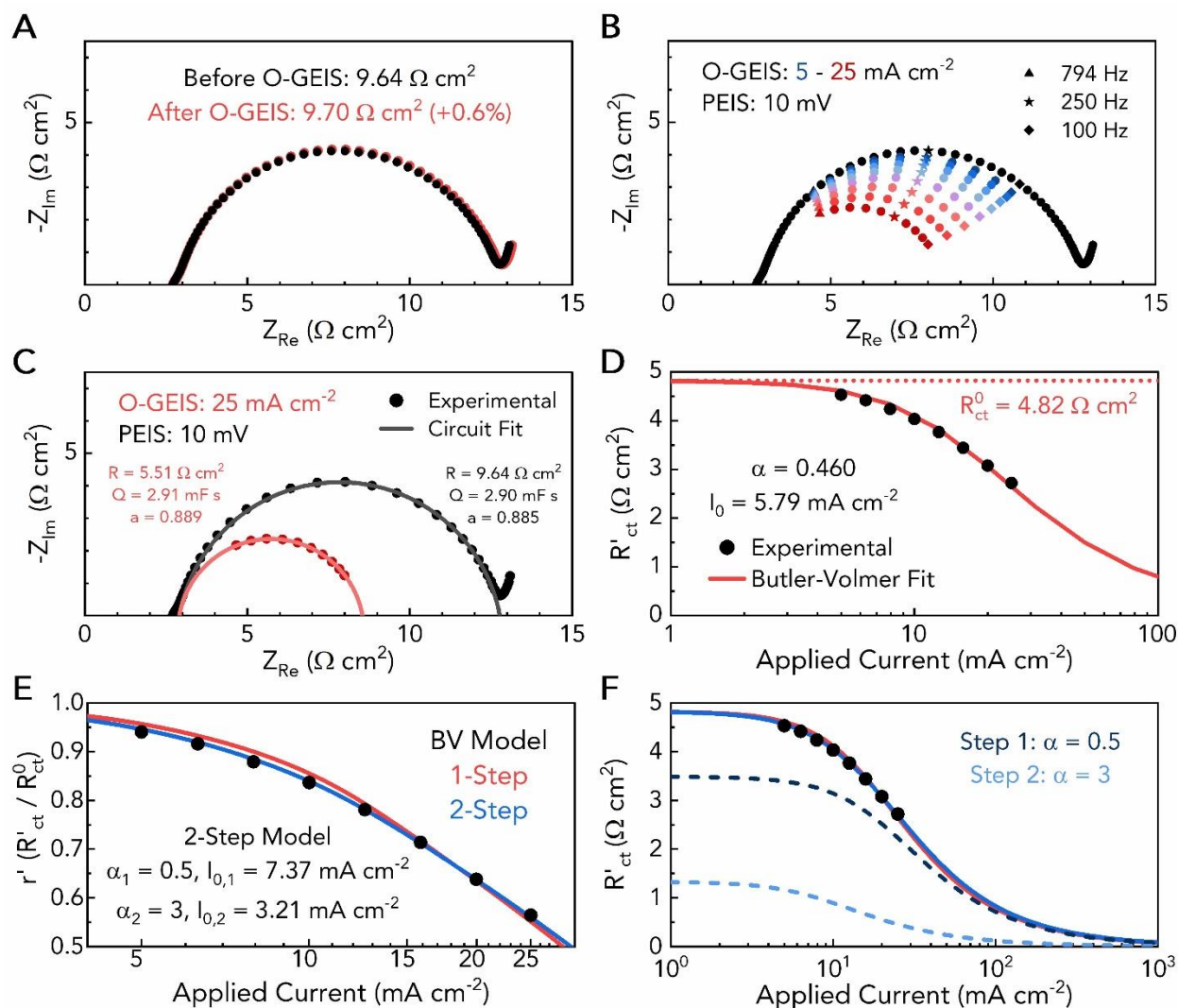
52

Figure 11. O-GEIS measurement results.
(**A**) PEIS spectra (500 kHz – 1 Hz) of an LCO symmetric cell collected before and after the O-GEIS measurements. (**B**) Nyquist plots of the raw impedance data collected from PEIS (500 kHz – 1 Hz), and O-GEIS (100 – 794 Hz) with applied currents of 5 – 25 mA cm^{-2} and a 10% current excitation. (**C**) Representative equivalent-circuit fits of the impedance spectra used to calculate R_{ct} from PEIS and O-GEIS measurements. The circuit model is $Z = R_\Omega + R_{ct}/Q$, and the value of R_Ω is measured with PEIS under blocking conditions. (**D**) Differential charge-transfer resistance (R'_{ct}) versus applied current data from O-GEIS measurements, fitted to a 1-step BV model (Eq. 40) with least squares error minimization to calculate the values of α and I_0. (**E**) Plot of normalized differential charge-transfer resistance (r') versus applied current, comparing the experimental data, a 2-step BV model (assuming $\alpha_1 = 0.5$ and $\alpha_2 = 3$) with $I_{0,1}$ and $I_{0,2}$ values calculated by least squares error minimization (Eqs. 23 and 39), and the 1-step BV model. (**F**) Calculated R'_{ct} versus current data from the fitted 2-step BV model, showing the contribution of each reaction step to the measured differential resistance.

53

current densities, are both highly consistent with a two-step reaction with $\alpha_1 = 0.5$ and $\alpha_2 = 3$. Therefore, the R'_{ct} versus current data were also fitted to a two-step BV model, assuming $\alpha_1 = 0.5$ and $\alpha_2 = 3$, to calculate the values of $I_{0,n}$ for each reaction step. The 2-step BV model fits the data more closely in the intermediate current range, yielding $I_{0,1} = 7.37$ mA cm^{-2} and $I_{0,2} = 3.21$ mA cm^{-2}. The contribution of each reaction step to the measured differential resistance (*i.e.*, $R'_{ct,n}$) can be calculated as a function of current from the fitted two-step BV model (Fig. 11F). Step 1 ($\alpha = 0.5$) accounts for most (78%) of the total linearized charge-transfer resistance compared, even though $I_{0,2} < I_{0,1}$. For Step 2, R'_{ct} also begins decreasing at a lower current density than for Step 1, so $R'_{ct,2}$ becomes negligible compared to $R'_{ct,1}$ at high current densities. However, since the exchange current between the two steps is similar, the overall resistance versus current density relation is not significantly different between the one-step and two-step BV models. In such a case, a one-step BV model may be a reasonable approximation. Overall, the O-GEIS data clearly fit the predicted relationship between differential charge-transfer resistance and current density for BV kinetics, but the data appear to be more consistent with a two-step reaction with $\alpha_1 = 0.5$ and $\alpha_2 = 3$, than with a one-step reaction with $\alpha \approx 0.46$.

5. Discussion

The BV equation predicts that the charge-transfer resistance and differential charge-transfer resistance should decrease with current density following a universal dimensionless relationship. Across all the electrochemical techniques investigated, the experimentally measured decrease in resistance as a function of current density is shown to be fully and quantitatively consistent with the BV equation. The finding that LCO obeys BV kinetics at high current densities can likely be broadly generalized to most other LIB AMs. The deviations from BV kinetics reported for LIB

AMs in the literature are probably caused by uncompensated ohmic resistance in the measurements [12–14,20]. Additionally, non-linearity during EIS measurements is typically avoided in the literature because it is believed to cause inaccurate analysis. However, we quantitatively show that both O-GEIS and LA-GEIS measurements can be conducted within the non-linear region of the kinetics, while maintaining a sufficiently linear impedance response. The decrease in interfacial impedance with increasing current is not an artifact or distortion of the EIS data; it is literally the non-linearity of BV kinetics, and this is something to be precisely and quantitatively measured, not to be avoided.

Surprisingly, the magnitude of the R_{ct}^0 was found to be a factor of $\sqrt{2}$ higher for S3E-CP measurements than for LA-GEIS and O-GEIS measurements. As a result, the measured I_0 values from LA-GEIS and O-GEIS are a factor of $\sqrt{2}$ higher than from S3E-CP. This difference does not appear to be caused by a problem with the potentiostat hardware or software; EIS and DC measurements of a 100 Ω R-C circuit on the potentiostat calibration board yielded the same resistance value. There appears to be a real difference in the magnitude of the measured resistance between EIS and DC techniques, which is likely an artifact of the EIS measurement. For example, if the current is not calculated on an RMS basis for LA-GEIS data analysis, then the I_0 value agrees with S3E-CP, but the α value disagrees by a factor of $\sqrt{2}$. For O-GEIS data analysis, it was empirically found that the applied DC bias must also be calculated on an RMS basis. It seems plausible that this discrepancy arises as an artifact of the RMS averaging which occurs during EIS measurement, but not during DC measurements [28]. Other differences in the magnitude of resistance measured between DC and EIS techniques have been shown in the literature. For

example, the measured electrode pore resistance is three times lower from EIS than from DC measurements [22]. We also previously showed that for nanosized $LiFePO_4$, R_{ct} is immeasurably small with EIS, but measurable with S3E-CP, due to differences in the active particle population dynamics between DC and EIS techniques [18]. To the best of our knowledge, there are no other reports in the literature directly comparing the magnitude of R_{ct}^0 measured between DC or EIS techniques. Considering that practical LIB operation occurs only under DC conditions, it may be necessary to quantitatively account for this difference in electrochemical models of LIBs. For example, if the model is parameterized with EIS measurements, it is possible that the resistance under real-world conditions may be underestimated by a factor of $\sqrt{2}$. Further investigation is needed to better understand the origins and consequences of this phenomenon.

There are undoubtedly many opportunities to further improve and extend the O-GEIS and LA-GEIS measurement techniques. Improved drift correction methods for O-GEIS could allow for accurate measurements at higher current densities and/or lower frequencies, which may be useful for some systems [57]. For example, it seems possible that a direct subtraction of the voltage versus time data between S3E-CP and O-GEIS measurements conducted under the same conditions, as shown by Fig. 7B, could be used to quantitatively account for voltage changes during the measurement. The experimental methods for LA-GEIS can easily be extended to the strongly non-linear region of the kinetics, although resistive heating may limit the maximum current excitation. However, the data would need to be analyzed with quantitative models for the non-linear impedance response to account for the harmonic distortions; this can be referred to as non-linear galvano EIS (NL-GEIS). One approach for NL-GEIS is to correct the impedance data for the distortions by subtracting the contributions of the disturbing terms at the fundamental frequency, which can be calculated with a Taylor series expansion from the experimentally

56

measured magnitudes of the harmonics [33,62]. Another approach for NL-GEIS is to directly calculate the BV kinetic parameters from the experimentally measured magnitudes of the harmonics with non-linear impedance models [30–32,67]. Exact expressions for the non-linear impedance response can likely be derived from a series expansion of the BV equation, which is infinitely differentiable [67,68]. Since linear processes like ohmic resistance do not generate harmonics, NL-GEIS may enable accurate measurements of the BV kinetic parameters without requiring explicit IR compensation [69]. NL-GEIS may also provide important information about the symmetry of the kinetics [67].

In the literature, it is nearly universally assumed that $\alpha \approx 0.5$ for the interfacial charge-transfer reactions in LIB AMs. In our previous work, however, S3E-CP measurements showed that $\alpha \approx 3$ for LFP [18]. In this work, $\alpha \approx 0.43$ was experimentally measured for LCO with LA-GEIS measurements at low current densities, and with S3E-CP measurements at high current densities. It was quantitatively shown that neither irreversible impedance growth, resistive heating, ohmic resistance, nor harmonic distortions are appreciable sources of error in the data analysis. Despite the differences in the measured I_0 values between EIS and DC techniques, there is excellent agreement between the α value measured with S3E-CP and LA-GEIS. It is extremely unlikely that this deviation from $\alpha \approx 0.5$ for LCO is a measurement error. An apparent α value of ~ 0.43 may seem at surface level to have little physical significance. However, the equations developed in this work predict that at either very high or very low current densities, a multi-step reaction will behave as a one-step reaction with apparent values of the BV kinetic parameters. The apparent α value for a two-step reaction with $\alpha_1 = 0.5$ and $\alpha_2 = 3$ is predicted to be 0.429, which agrees extremely well with the S3E-CP and LA-GEIS measurements in this work, and with S3E-CP measurements of LFP in our previous work [18]. Furthermore, the differential charge-transfer resistance

57

measurements from O-GEIS show that the data in the intermediate current range cannot be fit well by a one-step BV model, but are highly consistent with a two-step BV model. Overall, these findings suggest that the interfacial kinetics of the LCO studied in this work obey the BV equation for a two-step reaction with $\alpha_1 \approx 0.5$ and $\alpha_2 \approx 3$. However, these specific findings should not be generalized to other AMs and may not be broadly generalizable for LCO.

The common assumption of $\alpha = 0.5$ for the interfacial charge-transfer reaction in LIB AMs is based on the underlying assumption that electron transfer across the electrical double layer is the RDS for the interfacial charge-transfer reaction [7]. However, Peled's theory of the solid-electrolyte interphase (SEI) suggests that there are three possible reaction steps for the interfacial charge-transfer reaction in LIBs: (i) (de)solvation of Li^+ ions at the interface between the electrolyte and SEI, (ii) conduction of Li^+ ions through the electronically insulating SEI, and (iii) charge-transfer (*i.e.*, coupled ion/electron transfer) at the interface between the SEI and the AM [70,71]. An α value of ~ 3, as measured for LFP, is fundamentally inconsistent with electron-transfer as the RDS [7,18]. LFP is also thermodynamically stable with nearly all electrolytes, so unlike other AMs such as LCO or graphite, it does not form a passivating SEI layer due to reactions with the electrolyte [72]. Therefore, a reaction step with $\alpha = 3$ cannot plausibly be attributed to conduction of Li^+ ions through the SEI. As we proposed in our previous work, a reaction step with $\alpha = 3$ can most likely be attributed to (de)solvation of Li^+ ions at the interface between the electrolyte and the AM or SEI [18]. Therefore, a reaction step with $\alpha = 0.5$ for LCO could be attributed either to charge-transfer at the SEI/AM interface, or to Li^+ conduction through the SEI, but not to both. A reaction step with $\alpha = 0.5$ would be fully consistent with electron-transfer as the RDS [7]. However, assuming $\alpha = 0.5$ for electron-transfer, the measured α value would be < 0.43 if there were also appreciable resistances for both (de)solvation and SEI conduction. It is widely

known that due to their thermodynamic instability with the electrolyte at high SOC, lithium layered oxide cathodes typically form both a surface reconstruction (*i.e.*, rock-salt) layer, as well as a surface film of electrolyte decomposition products, which together constitute the SEI [43]. Numerous studies have shown that the interfacial resistance of layered oxide cathodes is strongly correlated to the thickness and composition of the SEI [73–75]. Based on the literature, a reaction step with $\alpha = 0.5$ for LCO could, therefore, also be plausibly attributed to Li^+ conduction through the SEI. Unfortunately, much more detailed studies would be required, including measurements on a wide range of LIB AMs, to make any more definitive conclusions about the mechanisms of interfacial charge-transfer in LIBs.

6. Conclusions

The Butler-Volmer equation was reformulated to describe the dependent of charge-transfer resistance (R_{ct}) on current density, showing that R_{ct} is constant for $I < I_0$, but decreases logarithmically with current at $I > I_0$. Expressions were derived for the differential charge-transfer resistance (R'_{ct}), which is the local slope of the overpotential-current curve at the applied current, and for the linearized charge-transfer resistance (R^0_{ct}), which is the limit of R'_{ct} as the current approaches zero. For a symmetric one-step reaction, it was shown that R_{ct} and R'_{ct} both follow universal dimensionless relationships between normalized resistance ($r = R_{ct}/R^0_{ct}$) and normalized current ($i = I/2I_0$), regardless of the specific values of α and I_0. These expressions were generalized for multi-step reactions, and it was shown that at either very low or very high current densities, or when I_0 is the same for all reaction steps, a multi-step reaction behaves analogously to a one-step reaction. However, when I_0 is different between the reaction steps, complex behaviors can arise as the resistance for each step decreases with a different current

59

dependency. Differential resistance measurements were shown to be best suited for investigating multi-step reactions due to the more rapid decrease of R'_{ct} than R_{ct} with increasing current.

LiCoO$_2$ symmetric cells were demonstrated as ideal model system for studying the interfacial charge-transfer kinetics in LIBs. Three electrochemical techniques were developed for high current density kinetic measurements: S3E-CP, LA-GEIS, and O-GEIS. S3E-CP works by extrapolating the voltage versus capacity data from short galvanostatic pulses to a capacity of zero to approximate steady-state conditions. LA-GEIS works by applying a large amplitude current excitation about the equilibrium voltage of the cell, while O-GEIS works by applying a small-amplitude current excitation about a much larger direct-current bias. O-GEIS, unlike the other two techniques, measures the differential charge-transfer resistance. The ohmic resistance was precisely measured with PEIS of separate symmetric cells under both blocking and interacting conditions to enable accurate IR compensation of the kinetic measurements. For each technique, it was quantitatively shown that the conditions of stability, stationarity, and linearity can be satisfactorily met with optimized measurement conditions. Although the interfacial resistance of LCO is highly sensitive to electrolyte impurities, the measurements appear to be generally non-destructive at current densities of up to 250 mA cm^{-2}. Due to the high activation energy for interfacial charge-transfer, extremely precise temperature control is needed for accurate measurements. At high current densities, even slight resistive heating of the cell (< 1°C) causes significant resistance changes, which can lead to inaccurate results, especially for LA-GEIS; this can be effectively mitigated with a limited current density and appropriate rest times between measurements. While S3E-CP and LA-GEIS are inherently stationary, O-GEIS measurements are sensitive to drift at high current densities and low frequencies; this can be mitigated by employing drift correction of the impedance data and limiting the measurements to high frequencies (*e.g.*, >

60

100 Hz). Due to the small excitation amplitude, the impedance response from O-GEIS measurements was shown to be highly linear, even when the measurements were conducted within the strongly non-linear region of the kinetics. Conversely, due to the large amplitude excitation of LA-GEIS, harmonic distortions of the impedance response render the linear impedance measurement inaccurate at high current densities; however, the total harmonic distortion is sufficiently low within the weakly non-linear region of the kinetics to obtain accurate LA-GEIS measurements.

S3E-CP measurements from $5 - 100$ mA cm^{-2} show that the experimental data are fully consistent with the BV equation for a one-step reaction with $\alpha = 0.422$ and $I_0 = 4.43$ mA cm^{-2}. LA-GEIS measurements from $1 - 10$ mA cm^{-2} also fit the BV equation with $\alpha = 0.431$ and $I_0 = 6.11$ mA cm^{-2}, although the experimental data deviates from the BV model at high current densities due to the harmonic distortions. Surprisingly, there is a $\sim \sqrt{2}$ different in the experimentally measured magnitude of R_{ct}^0, and therefore I_0, between direct-current and EIS techniques. This appears to be a physical phenomenon arising from the root-mean-square averaging of the impedance data. Since O-GEIS measurements involve both a DC and EIS component, this empirical difference must be accounted for to obtain an accurate analysis. O-GEIS measurements from $5 - 25$ mA cm^{-2} show that the measured R_{ct}' versus current data agree reasonably well with the BV equation for a one-step reaction with $\alpha = 0.460$ and $I_0 = 5.79$ mA cm^{-2}. However, a two-step BV model assuming $\alpha_1 = 0.5$ and $\alpha_2 = 3$ was shown to fit the data much more closely and allowed for deconvolution of the resistance for each reaction step based on the assumed α values. Overall, the S3E-CP, LA-GEIS, and O-GEIS measurements are all quantitatively consistent with a two-step charge-transfer reaction for LCO with transfer coefficients of $\alpha_1 = 0.5$ and $\alpha_2 = 3$. It is proposed that the reaction step with $\alpha = 3$ could be attributed to Li$^+$ (de)solvation at the SEI/electrolyte interface, while the

61

reaction step with $\alpha = 0.5$ could plausibly be attributed to either electron-transfer or Li^+ conduction through the SEI, but not to both. To the best of our knowledge, there are no existing theories in the literature which would quantitatively predict an α value for the (de)solvation or SEI conduction reactions in LIBs.

These findings clearly illustrate the need to conduct electrochemical kinetic measurements across a wide range of current densities, including high current densities, to fully characterize the interfacial charge-transfer kinetics of LIB AMs. The quantitative models developed herein for measuring the apparent α and I_0 values are universally generalizable to any electrochemical system, which obeys symmetric BV kinetics, although models must still be developed to treat the case of asymmetry. The experimental methods and electrochemical measurements techniques developed herein are expected to be broadly applicable for measuring the interfacial charge-transfer kinetics of rechargeable battery active materials, although their implementation will surely need to be modified for each specific system. Our measurement results obtained so far of $\alpha \approx 3$ for LFP and $\alpha \approx 0.43$ for LCO suggest that the mechanisms of interfacial charge-transfer in LIBs cannot be fully explained by the classical theories of electron-transfer. Furthermore, these results imply that there may be a significant diversity of the interfacial kinetic behaviors in LIBs. The physical mechanisms of interfacial charge-transfer in LIBs can hopefully be clarified by applying the methodology developed in this work to study a wide range of LIB AMs and electrolytes. This will be a topic of future work.

Acknowledgements

Author Contributions

Conceptualization, K. S.; Investigation, K. S.; Writing – Original Draft, K. S.; Writing – Review and Editing, A. M; Supervision, A. M.

Declaration of Interests

The authors declare no competing interests.

References

[1] J. Newman, W. Tiedemann, Porous-electrode theory with battery applications, AIChE J 21 (1975) 25–41. https://doi.org/10.1002/aic.690210103.

[2] C.-H. Chen, F. Brosa Planella, K. O'Regan, D. Gastol, W.D. Widanage, E. Kendrick, Development of Experimental Techniques for Parameterization of Multi-scale Lithium-ion Battery Models, J Electrochem Soc 167 (2020) 080534. https://doi.org/10.1149/1945-7111/ab9050.

[3] T.R. Garrick, Y. Zeng, J.B. Siegel, V.R. Subramanian, From Atoms to Wheels: The Role of Multi-Scale Modeling in the Future of Transportation Electrification, J Electrochem Soc 170 (2023) 113502. https://doi.org/10.1149/1945-7111/ad0919.

[4] M. Keyser, A. Pesaran, Q. Li, S. Santhanagopalan, K. Smith, E. Wood, S. Ahmed, I. Bloom, E. Dufek, M. Shirk, A. Meintz, C. Kreuzer, C. Michelbacher, A. Burnham, T. Stephens, J. Francfort, B. Carlson, J. Zhang, R. Vijayagopal, K. Hardy, F. Dias, M. Mohanpurkar, D. Scoffield, A.N. Jansen, T. Tanim, A. Markel, Enabling fast charging – Battery thermal considerations, J Power Sources 367 (2017) 228–236. https://doi.org/10.1016/j.jpowsour.2017.07.009.

[5] X. Li, A.M. Colclasure, D.P. Finegan, D. Ren, Y. Shi, X. Feng, L. Cao, Y. Yang, K. Smith, Degradation mechanisms of high capacity 18650 cells containing Si-graphite anode and nickel-rich NMC cathode, Electrochim Acta 297 (2019) 1109–1120. https://doi.org/10.1016/j.electacta.2018.11.194.

[6] N. Zhang, S. Yu, I. Hamam, B. Tang, M. Johnson, J.R. Dahn, Long-Term Cycling and Mechanisms of Cell Degradation of Single Crystal $LiNi_{0.95}Mn_{0.04}Co_{0.01}O_2$ /Graphite Cells, J Electrochem Soc 171 (2024) 010520. https://doi.org/10.1149/1945-7111/ad1d94.

[7] A.J. Bard, L.R. Faulkner, Electrochemical Methods: Fundamentals and Applications, Wiley, New York, 2000.

[8] E.J.F. Dickinson, A.J. Wain, The Butler-Volmer equation in electrochemical theory: Origins, value, and practical application, J Electroanal Chem 872 (2020) 114145. https://doi.org/10.1016/j.jelechem.2020.114145.

[9] M. Gaberšček, Understanding Li-based battery materials via electrochemical impedance spectroscopy, Nat Commun 12 (2021) 6513. https://doi.org/10.1038/s41467-021-26894-5.

[10] M. Gaberšček, Impedance spectroscopy of battery cells: theory versus experiment, Curr Opin Electrochem 32 (2021) 100917. https://doi.org/10.1016/j.coelec.2021.100917.

[11] A.C. Lazanas, M.I. Prodromidis, Electrochemical Impedance Spectroscopy ─ A Tutorial, ACS Meas. Sci. 3 (2023) 162–193. https://doi.org/10.1021/acsmeasuresciau.2c00070.

[12] A. Allagui, H. Benaoum, C. Wang, Deformed Butler-Volmer Models for Convex Semilogarithmic Current-Overpotential Profiles of Li-ion Batteries, J Phys Chem C 126 (2022) 3029–3036. https://doi.org/10.1021/asc.jpcc.1c09620.

[13] P. Bai, M.Z. Bazant, Charge transfer kinetics at the solid-solid interface in porous electrodes, Nat Commun 5 (2014) 1–7. https://doi.org/10.1038/ncomms4585.

[14] Y. Zhang, D. Fraggedakis, T. Gao, S. Pathak, D. Zhuang, C. Grosu, Y. Samantaray, A.R. Neto, S.R. Duggirala, B. Huang, Y. Guang Zhu, L. Giordano, R. Tatara, H. Agarwal, R.M. Stephens, M.Z. Bazant, Y. Shao-Horn, Lithium-ion intercalation by coupled ion-electron transfer, ChemRxiv (2024). https://doi.org/10.26434/chemrxiv-2024-d00cp-v2. *Preprint.*

[15] C. Heubner, M. Schneider, A. Michaelis, Investigation of charge transfer kinetics of Li-Intercalation in LiFePO$_4$, J Power Sources 288 (2015) 115–120. https://doi.org/10.1016/j.jpowsour.2015.04.103.

[16] N. Damay, K. Mergo Mbeya, G. Friedrich, C. Forgez, Separation of the charge transfers and solid electrolyte interphase contributions to a battery voltage by modeling their non-linearities regarding current and temperature, J Power Sources 516 (2021) 230617. https://doi.org/10.1016/j.jpowsour.2021.230617.

[17] D.T. Boyle, X. Kong, A. Pei, P.E. Rudnicki, F. Shi, W. Huang, Z. Bao, J. Qin, Y. Cui, Transient Voltammetry with Ultramicroelectrodes Reveals the Electron Transfer Kinetics of Lithium Metal Anodes, ACS Energy Lett 5 (2020) 701–709. https://doi.org/10.1021/acsenergylett.0c00031.

[18] K.P. Scanlan, A. Manthiram, Revealing the Electrochemical Kinetics of Electrolytes in Nanosized LiFePO$_4$ Electrodes, J Electrochem Soc 170 (2023) 100515. https://doi.org/10.1149/1945-7111/acfc69.

[19] K. Dokko, N. Nakata, Y. Suzuki, K. Kanamura, High-rate lithium deintercalation from lithiated graphite single-particle electrode, J Phys Chem C 114 (2010) 8646–8650. https://doi.org/10.1021/jp101166d.

[20] R. Xiong, M. Zhou, L. Li, J. Xu, M. Li, B. yan, D. Li, Y. Zhang, H. Zhou, Decoupled measurement and modeling of interface reaction kinetics of ion-intercalation battery electrodes, Energy Storage Mater 54 (2023) 836–844. https://doi.org/10.1016/j.ensm.2022.11.027.

[21] R.A. Marcus, On the Theory of Oxidation-Reduction Reactions Involving Electron Transfer, J Chem Phys 24 (1956) 966–978. https://doi.org/https://doi.org/10.1021/j100798a033.

[22] R. Morasch, J. Keilhofer, H.A. Gasteiger, B. Suthar, Methods—Understanding Porous Electrode Impedance and the Implications for the Impedance Analysis of Li-Ion Battery Electrodes, J Electrochem Soc 168 (2021) 080519. https://doi.org/10.1149/1945-7111/ac1892.

[23] M.C. Lefebvre, Establishing the Link Between Multistep Electrochemical Reaction Mechanisms and Experimental Tafel Slopes, in: B.E. Conway, J.O. Bockris, R.E. White (Eds.), Modern Aspects of Electrochemistry, 1st ed., Springer, New York, NY, 2002: pp. 249–300. https://doi.org/10.1007/0-306-46916-2_3.

[24] R. Guidelli, R.G. Compton, J.M. Feliu, E. Gileadi, J. Lipkowski, W. Schmickler, S. Trasatti, Defining the transfer coefficient in electrochemistry: An assessment (IUPAC Technical Report), Pure and Applied Chemistry 86 (2014) 245–258. https://doi.org/10.1515/pac-2014-5026.

[25] F.A. Posey, Methods for the Calculation of Polarization in Porous Electrodes, J Electrochem Soc 111 (1964) 1173. https://doi.org/10.1149/1.2425944.

[26] K. Darowicki, Linearization in impedance measurements, Electrochim Acta 42 (1997) 1781–1788. https://doi.org/10.1016/S0013-4686(96)00377-5.

[27] B. Hirschorn, B. Tribollet, M.E. Orazem, On Selection of the Perturbation Amplitude Required to Avoid Nonlinear Effects in Impedance Measurements, Isr J Chem 48 (2008) 133–142. https://doi.org/10.1560/ijc.48.3-4.133.

[28] K. Darowicki, The Amplitude Analysis of Impedance Spectra, Electrochim Acta 40 (1995) 439–445. https://doi.org/10.1016/0013-4686(94)00303-I.

[29] J.S. Newman, C.W. Tobias, Theoretical Analysis of Current Distribution in Porous Electrodes, J Electrochem Soc 109 (1962) 1183. https://doi.org/10.1149/1.2425269.

[30] N. Hallemans, D. Howey, A. Battistel, N.F. Saniee, F. Scarpioni, B. Wouters, F. La Mantia, A. Hubin, W.D. Widanage, J. Lataire, Electrochemical impedance spectroscopy beyond linearity and stationarity—A critical review, Electrochim Acta 466 (2023) 142939. https://doi.org/10.1016/j.electacta.2023.142939.

[31] N. Wolff, N. Harting, F. Röder, M. Heinrich, U. Krewer, Understanding nonlinearity in electrochemical systems, Euro Phys J: Special Topics 227 (2019) 2617–2640. https://doi.org/10.1140/epjst/e2019-800135-2.

[32] T.J. McDonald, S. Adler, (Invited) Theory and Application of Nonlinear Electrochemical Impedance Spectroscopy, ECS Trans 45 (2012) 429–439. https://doi.org/10.1149/1.3701334.

[33] M. Kiel, O. Bohlen, D.U. Sauer, Harmonic analysis for identification of nonlinearities in impedance spectroscopy, Electrochim Acta 53 (2008) 7367–7374. https://doi.org/10.1016/j.electacta.2008.01.089.

[34] E. Barsoukov, J.R. Macdonald, Impedance Spectroscopy: Theory, Experiment, and Applications, Wiley, 2005. https://doi.org/10.1002/9781119381860.

[35] N. Ogihara, Y. Itou, T. Sasaki, Y. Takeuchi, Impedance spectroscopy characterization of porous electrodes under different electrode thickness using a symmetric cell for high-performance lithium-ion batteries, J Phyl Chem C 119 (2015) 4612–4619. https://doi.org/10.1021/jp512564f.

[36] K. Kisu, S. Aoyagi, H. Nagatomo, E. Iwama, M.T.H. Reid, W. Naoi, K. Naoi, Internal resistance mapping preparation to optimize electrode thickness and density using symmetric cell for high-performance lithium-ion batteries and capacitors, J Power Sources 396 (2018) 207–212. https://doi.org/10.1016/j.jpowsour.2018.05.083.

[37] X. Li, L. Zhou, H. Wang, D. Meng, G. Qian, Y. Wang, Y. He, Y. Wu, Z. Hong, Z.F. Ma, L. Li, Dopants modulate crystal growth in molten salts enabled by surface energy tuning, J Mater Chem A 9 (2021) 19675–19680. https://doi.org/10.1039/d1ta02351a.

[38] S. Oswald, M. Bock, H.A. Gasteiger, The Implications of Particle Morphology on the Capacity Retention, Side Reactions, and Impedance Build-Up of Nickel-Rich NCMs upon Cycling in Full-Cells: Poly- vs. Single-Crystalline NCM851005, J Electrochem Soc 170 (2023) 090505. https://doi.org/10.1149/1945-7111/acf3a1.

[39] S. Oswald, D. Pritzl, M. Wetjen, H.A. Gasteiger, Novel Method for Monitoring the Electrochemical Capacitance by In Situ Impedance Spectroscopy as Indicator for Particle Cracking of Nickel-Rich NCMs: Part I. Theory and Validation, J Electrochem Soc 167 (2020) 100511. https://doi.org/10.1149/1945-7111/ab9187.

[40] M. Gaberscek, J. Moskon, B. Erjavec, R. Dominko, J. Jamnik, The importance of interphase contacts in Li ion electrodes: The meaning of the high-frequency impedance arc, Electrochemical and Solid-State Letters 11 (2008) 170–174. https://doi.org/10.1149/1.2964220.

[41] D. Pritzl, A.E. Bumberger, M. Wetjen, J. Landesfeind, S. Solchenbach, H.A. Gasteiger, Identifying Contact Resistances in High-Voltage Cathodes by Impedance Spectroscopy, J Electrochem Soc 166 (2019) A582–A590. https://doi.org/10.1149/2.0451904jes.

[42] J. Illig, M. Ender, T. Chrobak, J.P. Schmidt, D. Klotz, E. Ivers-Tiffée, Separation of Charge Transfer and Contact Resistance in $LiFePO_4$ Cathodes by Impedance Modeling, J Electrochem Soc 159 (2012) A952–A960. https://doi.org/10.1149/2.030207jes.

[43] R. Konar, S. Maiti, N. Shpigel, D. Aurbach, Reviewing failure mechanisms and modification strategies in stabilizing high-voltage $LiCoO_2$ cathodes beyond 4.55V, Energy Storage Mater 63 (2023) 103001. https://doi.org/10.1016/j.ensm.2023.103001.

[44] L. Ma, L. Ellis, S.L. Glazier, X. Ma, J.R. Dahn, Combinations of $LiPO_2F_2$ and Other Electrolyte Additives in $Li[Ni_{0.5}Mn_{0.3}Co_{0.2}]O_2$ /Graphite Pouch Cells , J Electrochem Soc 165 (2018) A1718–A1724. https://doi.org/10.1149/2.0661809jes.

[45] T. Teufl, D.J. Pritzl, L. Hartmann, S. Solchenbach, M. Mendez, H. Gasteiger, Implications of the Thermal Stability of FEC-Based Electrolytes for Li-Ion Batteries, J Electrochem Soc 170 (2023) 020531. https://doi.org/10.1149/1945-7111/acbc52.

[46] H. Nara, K. Morita, T. Yokoshima, D. Mukoyama, T. Momma, T. Osaka, Electrochemical impedance spectroscopy analysis with a symmetric cell for $LiCoO_2$ cathode degradation correlated with Co dissolution, AIMS Mater Sci 3 (2016) 448–459. https://doi.org/10.3934/matersci.2016.2.448.

[47] D. Strmcnik, I.E. Castelli, J.G. Connell, D. Haering, M. Zorko, P. Martins, P.P. Lopes, B. Genorio, T. Østergaard, H.A. Gasteiger, F. Maglia, B.K. Antonopoulos, V.R. Stamenkovic, J. Rossmeisl, N.M. Markovic, Electrocatalytic transformation of HF impurity to H_2 and LiF in lithium-ion batteries, Nat Catal 1 (2018) 255–262. https://doi.org/10.1038/s41929-018-0047-z.

[48] S.D. Talian, S. Brutti, M.A. Navarra, J. Moskon, M. Gaberscek, Impedance spectroscopy applied to lithium battery materials: Good practices in measurements and analyses, Energy Storage Mater 69 (2024) 103413. https://doi.org/10.1016/j.ensm.2024.103413.

[49] C. Heubner, S. Maletti, O. Lohrberg, T. Lein, T. Liebmann, A. Nickol, M. Schneider, A. Michaelis, Electrochemical Characterization of Battery Materials in 2-Electrode Half-Cell Configuration: A Balancing Act Between Simplicity and Pitfalls, Batter Supercaps 4 (2021) 1310–1322. https://doi.org/10.1002/batt.202100075.

[50] R. Morasch, B. Suthar, H.A. Gasteiger, Simple Way of Making Free-Standing Battery Electrodes and their Use in Enabling Half-Cell Impedance Measurements via μ-Reference Electrode, J Electrochem Soc 167 (2020) 100540. https://doi.org/10.1149/1945-7111/ab9b93.

[51] C. Bünzli, H. Kaiser, P. Novák, Important Aspects for Reliable Electrochemical Impedance Spectroscopy Measurements of Li-Ion Battery Electrodes, J Electrochem Soc 162 (2015) A218–A222. https://doi.org/10.1149/2.1061501jes.

[52] M. Ender, J. Illig, E. Ivers-Tiffée, J. Costard, M. Ender, M. Weiss, E. Ivers-Tiffée, Three-Electrode Setups for Lithium-Ion Batteries, J Electrochem Soc 164 (2017) A80–A87. https://doi.org/10.1149/2.0241702jes.

[53] S. Klink, E. Madej, E. Ventosa, A. Lindner, W. Schuhmann, F. La Mantia, The importance of cell geometry for electrochemical impedance spectroscopy in three-electrode lithium ion battery test cells, Electrochem Commun 22 (2012) 120–123. https://doi.org/10.1016/j.elecom.2012.06.010.

[54] R. Morasch, H.A. Gasteiger, B. Suthar, Li-Ion Battery Material Impedance Analysis II: Graphite and Solid Electrolyte Interphase Kinetics, J Electrochem Soc 171 (2024) 050548. https://doi.org/10.1149/1945-7111/ad48c0.

[55] R. Morasch, H.A. Gasteiger, B. Suthar, Li-Ion Battery Active Material Impedance Analysis I: Comparison of Measured NCM 111 Kinetics with Butler-Volmer Equation Based Predictions, J Electrochem Soc 170 (2023) 080522. https://doi.org/10.1149/1945-7111/acf161.

[56] J.C. Burns, L.J. Krause, D.-B. Le, L.D. Jensen, A.J. Smith, D. Xiong, J.R. Dahn, Introducing Symmetric Li-Ion Cells as a Tool to Study Cell Degradation Mechanisms, J Electrochem Soc 158 (2011) A1417. https://doi.org/10.1149/2.084112jes.

[57] M.E. Orazem, B. Ulgut, On the use of drift correction for electrochemical impedance spectroscopy measurements, Electrochim Acta 443 (2023) 141959. https://doi.org/10.1016/j.electacta.2023.141959.

[58] J. Huang, J. Zhang, Theory of Impedance Response of Porous Electrodes: Simplifications, Inhomogeneities, Non-Stationarities and Applications, J Electrochem Soc 163 (2016) A1983–A2000. https://doi.org/10.1149/2.0901609jes.

[59] J. Huang, H. Ge, Z. Li, J. Zhang, Dynamic Electrochemical Impedance Spectroscopy of a Three Electrode Lithium-Ion Battery during Pulse Charge and Discharge, Electrochim Acta 176 (2015) 311–320. https://doi.org/10.1016/j.electacta.2015.07.017.

[60] B. Hirschorn, M.E. Orazem, On the Sensitivity of the Kramers–Kronig Relations to Nonlinear Effects in Impedance Measurements, J Electrochem Soc 156 (2009) C345. https://doi.org/10.1149/1.3190160.

[61] J. Min Goh, C. Eluagu, J. Babauta, M.E. Orazem, Comparison of Approaches for Assessing Linearity of Impedance Measurements, J Electrochem Soc 171 (2024) 036508. https://doi.org/10.1149/1945-7111/ad3581.

[62] J.-P. Diard, B. Le Gorrec, C. Montella, Deviation from the polarization resistance due to non-linearity I - theoretical formulation, J Electroanal Chem 432 (1997) 27–30. https://doi.org/10.1016/S0022-0728(97)00213-1.

[63] G. Katırcı, M.A. Zabara, B. Ülgüt, Methods—Unexpected Effects in Galvanostatic EIS of Randles' Cells: Initial Transients and Harmonics Generated, J Electrochem Soc 169 (2022) 030527. https://doi.org/10.1149/1945-7111/ac5ad7.

[64] M.A. Zabara, J.M. Goh, V.M. Gaudio, L. Zou, M.E. Orazem, B. Ulgut, Utility of Lissajous Plots for Electrochemical Impedance Spectroscopy Measurements: Detection of Non-Linearity and Non-Stationarity, J Electrochem Soc 171 (2024) 010507. https://doi.org/10.1149/1945-7111/ad19eb.

[65] J.P. Diard, B. Le Gorrec, C. Montella, Theoretical formulation of the odd harmonic test criterion for EIS measurements, J Electroanal Chem 377 (1994) 61–73. https://doi.org/10.1016/0022-0728(94)03624-1.

[66] P. Delahay, G.G. Susbielles, Double-Layer Impedance of Electrodes with Charge-Transfer Reaction, J Phys Chem 70 (1966) 3150–3157. https://doi.org/10.1021/j100882a023.

[67] M.D. Murbach, V.W. Hu, D.T. Schwartz, Nonlinear Electrochemical Impedance Spectroscopy of Lithium-Ion Batteries: Experimental Approach, Analysis, and Initial Findings, J Electrochem Soc 165 (2018) A2758–A2765. https://doi.org/10.1149/2.0711811jes.

[68] J.B. Diard Le Gorrec, C. Montella, Non-linear impedance for a two-step electrode reaction with an intermediate adsorbed species, Electrochim Acta 42 (1997) 1053–1072. https://doi.org/10.1016/S0013-4686(96)00206-X.

[69] J.-P. Diard, B. Le Gorrec, C. Montella, Deviation of the polarization resistance due to non-linearity II. Application to electrochemical reactions, J Electroanal Chem 432 (1997) 41–52. https://doi.org/10.1016/S0022-0728(97)00234-9.

[70] E. Peled, The Electrochemical Behavior of Alkali and Alkaline Earth Metals in Nonaqueous Battery Systems—The Solid Electrolyte Interphase Model, J Electrochem Soc 126 (1979) 2047–2051. https://doi.org/10.1149/1.2128859.

[71] E. Peled, S. Menkin, Review—SEI: Past, Present and Future, J Electrochem Soc 164 (2017) A1703–A1719. https://doi.org/10.1149/2.1441707jes.

[72] S. Malmgren, H. Rensmo, T. Gustafsson, M. Gorgoi, K. Edström, Nondestructive Depth Profiling of the Solid Electrolyte Interphase on $LiFePO_4$ and Graphite Electrodes, ECS Trans 25 (2010) 201–210. https://doi.org/10.1149/1.3393856.

[73] W.M. Dose, I. Temprano, J.P. Allen, E. Björklund, C.A. O'Keefe, W. Li, B.L. Mehdi, R.S. Weatherup, M.F.L. De Volder, C.P. Grey, Electrolyte Reactivity at the Charged Ni-Rich Cathode Interface and Degradation in Li-Ion Batteries, ACS Appl Mater Interfaces 14 (2022) 13206–13222. https://doi.org/10.1021/acsami.1c22812.

[74] A.S. Keefe, R. Weber, I.G. Hill, J.R. Dahn, Studies of the SEI layers in $Li(Ni_{0.5}Mn_{0.3}Co_{0.2})O_2$ /Artificial Graphite Cells after Formation and after Cycling, J Electrochem Soc 167 (2020) 120507. https://doi.org/10.1149/1945-7111/abaa1b.

[75] L. Ma, S. Young, L.D. Ellis, Q. Huang, X. Ma, M. Chatzidakis, H. Li, L. Thompson, A. Eldesoky, C.R.M. McFarlane, G.A. Botton, I.G. Hill, J.R. Dahn, Impact of a Titanium-Based Surface Coating Applied to $Li[Ni_{0.5}Mn_{0.3}Co_{0.2}]O_2$ on Lithium-Ion Cell Performance, ACS Appl Energy Mater 1 (2018) 7052–7064. https://doi.org/10.1021/acsaem.8b01472.